Commun Nonlinear Sci Numer Simulat 79 (2019) 104934

Contents lists available at ScienceDirect

Commun Nonlinear Sci Numer Simulat

journal homepage: www.elsevier.com/locate/cnsns

Research paper

Numerical simulation of dam-break flow impacting a stationary obstacle by a CLSVOF/IB method

C.H. Yu[a], H.L. Wen[b], Z.H. Gu[c], R.D. An[a,*]

[a] State key lab of Hydraulics and Mountain River Engineering, Sichuan University, China
[b] Department of Engineering Science and Ocean Engineering, National Taiwan University, China
[c] College of Civil Engineering and Architecture, Zhejiang University, Hangzhou, China

ARTICLE INFO

Article history:
Received 23 November 2018
Revised 24 July 2019
Accepted 30 July 2019
Available online 01 August 2019

Keywords:
Level set method
Volume of fluid method
Immersed boundary method
Dam-break flow
Navier-Stokes equations

ABSTRACT

In this paper we develop a Coupled Level Set and Volume Of Fluid and Immersed Boundary (CLSVOF/IB) method, and apply it to simulating the interaction between dam-break flow and stationary obstacles. The projection method which adopts the second-order Adams–Bashforth algorithm is performed for solving the Navier-Stokes equations on a fixed staggered Cartesian grid. The Point Successive Over-Relaxation (PSOR) method is then employed to solve the discretized linear system of the Poisson pressure equation. For fluid-fluid interface treatment, the CLSVOF model is implemented using the Tangent of Hyperbola for INterface Capturing (THINC) scheme with the Weighted Linear Interface Calculation (WLIC), and the level set function which is a distance function is used to calculate interface normal vectors. For solid-fluid interface treatment, we adopt the direct forcing IB method which can be easily extended to three-dimensional simulations. The artificial momentum forcing term is applied at certain points in cells containing both fluid and solid, which imposes a velocity condition to drive the solid body motion. The proposed CLSVOF/IB model is used to simulate dam-break flow and its interaction with stationary structures, and the results agree well with numerical and experimental data in the literature.

1. Introduction

Dams are important constructions for storing water and they also provide benefits such as flood protection, water supply, and hydropower generation. Investigation of dam-break flow has wide applications in the field of ocean and civil engineering [1–3]. If a dam breaks, the flood can cause significant losses of human life and properties, serious damages can arise from the high loads acting on structures, and even their stability can be compromised. Over the past few decades, numerical modeling has been well accepted as an effective method to understand the dam-break flow dynamics [4–6]. For example, Larocque et al. [7] conduct three-dimensional (3D) numerical simulations of dam-break flow by adopting the Large Eddy Simulations (LES), and the $k-\epsilon$ turbulence model in combination with capturing the free surface by the volume of fluid method. To further investigate the dam break induced flood events that can have damaging consequences, Aureli et al. [8] estimate the impact load exerted by dam break wave on an obstacle calculated from three different models, i.e., a 2D depth-averaged model, a 3D Eulerian two-phase model, and a 3D Smoothed Particle Hydrodynamics (SPH) model.

* Corresponding author.
E-mail address: anruidong@scu.edu.cn (R.D. An).

https://doi.org/10.1016/j.cnsns.2019.104934
1007-5704/

The main concerns regarding water impact phenomena in numerical simulations include the treatment of fluid-fluid and solid-fluid interfaces [9,10]. The fluid-fluid interface involving large interface distortions and complex topological changes such as wave breaking and spray formation can be simulated by adopting the corresponding interface–capturing method governing the evolution of free surface [11,12]. Well-known interface-capturing methods which advect the corresponding phase functions have been developed including the volume of fluid (VOF) method [13–15] and level set (LS) method [16–20]. Although VOF method has an excellent mass-conservation property, capturing the fluid-fluid interface by this method has been known to have computational difficulties. One of the difficulties is associated with the discontinuous spatial derivative of the VOF function near the interface. Thus, accuracy should be taken into consideration when calculating the normal and curvature. The other difficulty is the construction of interfaces involving complicated geometries [14].

When tracking moving interfaces for three-dimensional two-phase flows, the level set method which can provide accurate curvature and surface tension force can be efficiently used. This method, therefore, has been extensively adopted for wide applications including moving solid problems [21], bubble growth in microchannel [22], bubble rising in magnetic fields [23] and droplet penetration into a porous medium [24]. The level set method in [25] is also applicable to problems involving not only a complicated interface geometry but also a large density ratio. Implementation of this method should adopt high-order discretization schemes to solve level set equations, and a re-initialization step is suggested for better mass conservation. Otherwise, inaccurate capturing of dynamic interfaces may be induced [26,27]. To resolve the mass loss problem, other level set approaches have been developed to accurately capture the fluid-fluid interface, including the conservative level set (CLS) method [28–32], hybrid particle level set (HPLS) method [33,34], coupled volume of fluid and level set (VOSET) method [35–38], and coupled level set and volume of fluid (CLSVOF) method [39].

One of the most attractive methods is CLSVOF, which combines the advantages of both VOF (mass conservation) and LS (interface sharpness). Refs. [39–42] achieve the coupling by advecting the interface using the conservative VOF function, calculating the interface normal using the smoothed LS function, and updating the physical properties from a smoothed Heaviside function. The coupling can also be achieved using different strategies regarding the advection equations and the re-initialization procedure [43–46]. This coupling method is used for studying droplet impacting a dry surface [47], bubble growth and detachment [48] and plunging breaking waves [11,49].

To simulate solid-fluid interface problems involving stationary or moving bodies which are geometrically complex, the immersed boundary (IB) method can be adopted. IB is applicable to problems with irregular solid objects and does not necessarily have to conform to Cartesian grids. Since the grid does not necessarily conform to the solid boundary, the governing equations near the boundary should be modified by imposing a proper boundary condition. According to the review paper of Mittal and Iaccarino [50], the immersed boundary method can be generally categorized into two classes, the continuous forcing and the discrete forcing. In the continuous forcing method, an explicit forcing term is introduced to the continuous Navier-Stokes equations before discretization. Typical examples can be seen in the original method of Peskin [51]. In comparison with the continuous forcing IB method, a sharper representation of the immersed boundary is allowed in the discrete forcing method [52]. In the discrete forcing method, the forcing term can be either explicitly or implicitly applied to the discretized Navier-Stokes equations [53–55].

In the last ten years, numerous investigations have been carried out for simulation of multi-phase problems by using interface capturing/immersed boundary methods. Yang and Stern develop a sharp interface IB/LS method for wave-body interaction in Cartesian grids [10]. A sharp interface IB/VOF model which introduces wave generating and absorbing options is proposed for simulation of wave-structure interaction [56]. There exist a wide variety of similar algorithms which simulate water entry and exit, such as LS/IB method [57] and IB/CLSVOF method [58].

The highlight of this paper is the proposal of a simple CLSVOF method and a practical IB method for the treatment of fluid-fluid and fluid-solid problems respectively, which is then used to simulate dam-break flows impacting downstream obstacles. The highlights are detailed as follows: (1) In almost all CLSVOF methods, the operational split method [9,11,39–42] is used in the solution of the VOF and LS advection equations. In those CLSVOF methods, the advection equations are solved in each spatial coordinate direction one by one at each time step. Before solution of advection equations in the next spatial direction, solutions in the previous spatial direction are required for geometric reconstruction and re-initialization, which requires additional computational power. In the present CLSVOF method, the operational split method is used for the advection of the C (VOF function), but is not used in the ϕ (LS function). Following the advection of ϕ and C, re-initialization procedure is then performed to ensure that the two interfaces predicted by ϕ and C should be close to each other. (2) Since grid lines are not necessarily aligned with the boundary, interpolation is essential in IB methods. To this end, some algebraic type interpolation approaches have been proposed in the literature [10,56,57], which, on the other hand, however, may lead to numerical instabilities [10,56,57]. Without using complex interpolation techniques, the present study calculates momentum forcing terms using the volume fraction of solid on the body surface, and its implementation is easy for extension to three-dimensional cases.

This paper is organized as follows. In Section 2.1, governing equations are presented for the two immiscible fluids by using the LS method. Section 2.2 describes the dimensional splitting algorithm of the VOF equation. A CLSVOF algorithm is given in Section 2.3. In Section 3, the VOF advection equation is solved using the Tangent of Hyperbola for INterface Capturing/Weighed Linear Interface Calculation (THINC/WLIC) scheme, and LS is solved directly from its advection equation by the high-resolution Optimized Compact Reconstruction Weighted Essentially Non-Oscillatory (OCRWENO) scheme. The IB method is introduced in this section as well. Sections 4 and 5 present the numerical results of dam-break flows with/without obstacles using the Adams-Bashforth algorithm on staggered Cartesian grids. The conclusions are drawn in Section 6.

2. Mathematical model

2.1. Level set (LS) method

2.1.1. Initialization step

The LS method uses a level set function that is a signed distance function with a distance unit equal to the grid spacing to determine the position of the gas/liquid interface (with $\phi > 0$ in the liquid, $\phi < 0$ in the gas and the zero level set $\phi = 0$ in the gas/liquid interface). To keep ϕ as a signed distance function (i.e. satisfy $|\nabla\phi| = 1$), an initialization step is required to calculate the ϕ values of the points away from the interface by solving the following initialization equation to reach a steady state [17]:

$$\frac{\partial\phi}{\partial\tau} + \bar{S}(\phi_0)(|\nabla\phi| - 1) = 0, \tag{1}$$

where τ is the artificial time and $\phi_0 = \phi(\mathbf{x}, \tau = 0)$ is the level set function calculated at $\tau = 0$. $\bar{S}(\phi_0)$ in Eq. (1) denotes the smoothed sign function

$$\bar{S}(\phi_0) = 2\left(\bar{H}(\phi_0) - 0.5\right), \tag{2}$$

with

$$\bar{H}(\phi_0) = \begin{cases} 0 & ; \ if \ \ \phi_0 < -\varepsilon \\ \frac{1}{2}[1 + \frac{\phi_0}{\varepsilon} + \frac{1}{\pi}\sin(\frac{\pi\phi_0}{\varepsilon})] & ; \ if \ \ |\phi_0| \le \varepsilon \\ 1 & ; \ if \ \ \phi_0 > \varepsilon, \end{cases} \tag{3}$$

where ε is chosen to be $1.5\Delta x$ and Δx indicates the grid spacing. A steady-state solution to Eq. (1) can be obtained at time $T = L_D$, the largest length of the computational domain when solving Eq. (1). Eq. (1) improves $|\nabla\phi| = 1$ by correcting the deviations from it without changing the shape of the zero level set. The following exact distance field $\bar{d}$ is the steady-state solution to Eq. (1):

$$\phi(\mathbf{x}, \tau) = \begin{cases} \bar{d}; & for \ \ \mathbf{x} \in \text{the liquid} \\ 0; & for \ \ \mathbf{x} \in \psi \\ -\bar{d}; & for \ \ \mathbf{x} \in \text{the gas}. \end{cases} \tag{4}$$

2.1.2. Advection step

The evolution of the gas/liquid interface can be tracked by solving the following level set evolution equation:

$$\frac{\partial\phi}{\partial t} + \mathbf{u}\cdot\nabla\phi = 0, \tag{5}$$

where $\mathbf{u}$ denotes the fluid velocity field obtained by solving the Navier-Stokes equations. Eq. (5) can be expressed in the conservative form since $\mathbf{u}$ is divergence-free

$$\frac{\partial\phi}{\partial t} + \nabla\cdot(\mathbf{u}\phi) = 0. \tag{6}$$

Using a uniform grid in three space dimensions as example, Eq. (6) results in an ordinary differential equation by semi-discrete conservative finite difference scheme

$$\frac{d\phi_{i,j}}{dt} = -\frac{1}{\Delta x}(F_{i+\frac{1}{2},j,k} - F_{i-\frac{1}{2},j,k}) - \frac{1}{\Delta y}(G_{i,j+\frac{1}{2},k} - G_{i,j-\frac{1}{2},k}) - \frac{1}{\Delta z}(H_{i,j,k+\frac{1}{2}} - H_{i,j,k-\frac{1}{2}}), \tag{7}$$

where Δx, Δy, Δz are grid spacings in $x-$ direction, $y-$ direction and $z-$ direction, respectively. The approximation to the numerical fluxes $F_{i+\frac{1}{2},j,k}, G_{i,j+\frac{1}{2},k}, H_{i,j,k+\frac{1}{2}}$ at point $x_{i+\frac{1}{2},j,k}, y_{i,j+\frac{1}{2},k}, z_{i,j,k+\frac{1}{2}}$ from the discrete values of $F = u\phi, G = v\phi, H = w\phi$ can be reconstructed by a fourth-order OCRWENO scheme described in Section 3.1.1.

2.1.3. Re-initialization step

As computation marches, the level set function ϕ is no longer a signed distance function [19]. To keep ϕ as a signed distance function, the re-initialization procedure is needed. In the re-initialization procedure by solving Eq. (8), the position of the zero level set $\phi = 0$ should remain still. In practice, however, this may not be satisfied in numerical computation. The level set method is known to suffer from poor mass conservation performance because of the unintentional move of the zero level set during the re-initialization procedure. In order to conserve mass as much as possible, a mass correction term $\lambda\delta(\phi)|\nabla\phi|$ is thus introduced into Eq. (8)

$$\frac{\partial\phi}{\partial\tau} = \bar{S}(\phi_0)(1 - |\nabla\phi|) + \lambda\delta(\phi)|\nabla\phi|, \tag{8}$$

with

$$\lambda = -\frac{\int_\Omega \delta(\phi)(\bar{S}(\phi_0)(1 - |\nabla\phi|))d\Omega}{\int_\Omega \delta^2(\phi)|\nabla\phi|d\Omega}, \tag{9}$$

where Ω is computational domain and delta function $\delta(\phi)$ is given as:

$$\delta(\phi) = \begin{cases} \frac{1}{2\varepsilon}(1+cos(\frac{\pi\phi}{\varepsilon})) & ;\ if\ \ |\phi| < \varepsilon; \\ 0 & ;\ otherwise. \end{cases} \tag{10}$$

Numerical integration over the domain Ω in Eq. (9) in three dimensions is calculated by

$$\int_{\Omega_{ijk}} g\ d\Omega \approx \frac{h^3}{77}\left(51g(i,j,k) + \sum_{m,n,l=-1;(m,n,l)\neq(0,0,0)}^{1} g_{i+m,j+n,k+l}\right) \tag{11}$$

The derivation is detailed in Appendix. The re-initialization step is also needed in order to accurately calculate the interface surface normals in the THINC/WLIC scheme.

2.2. Volume of fluid method

The interface in VOF method is represented by a characteristic function χ given below in three-dimensional cases

$$\chi(x,y,z) = \begin{cases} 1; & for\ \ (x,y,z) \in \text{the liquid}, \\ -1; & for\ \ (x,y,z) \in \text{the gas}. \end{cases} \tag{12}$$

The fraction function or color function C, an integral of the phase's characteristic function χ, is used

$$C_{i,j} = \frac{1}{\Delta x\Delta y\Delta z}\int_0^{\Delta x}\int_0^{\Delta y}\int_0^{\Delta z}\chi(x,y,z)dxdydz. \tag{13}$$

The characteristic function χ is passively advected owing to its zero substantial derivative by the following equation

$$\frac{\partial\chi}{\partial t} + \nabla\cdot(\mathbf{u}\chi) - \chi\nabla\cdot\mathbf{u} = 0. \tag{14}$$

For the model Eq. (14), in this study, the dimensional splitting algorithm, which calculates fluxes separately along axes and performs three separate advections, is applied at an interior point (i, j, k) [59]:

$$C^*_{i,j,k} = C^n_{i,j,k} - \frac{F^n_{x,i+1/2,j,k} - F^n_{x,i-1/2,j,k}}{\Delta x} - C^n_{i,j,k}\frac{u_{i+1/2,j,k} - u_{i-1/2,j,k}}{\Delta x}\Delta t, \tag{15}$$

$$C^{**}_{i,j,k} = C^*_{i,j,k} - \frac{F^*_{y,i,j+1/2,k} - F^*_{y,i,j-1/2,k}}{\Delta y} - C^n_{i,j,k}\frac{v_{i,j+1/2,k} - v_{i,j-1/2,k}}{\Delta y}\Delta t, \tag{16}$$

$$C^{n+1}_{i,j,k} = C^{**}_{i,j,k} - \frac{F^{**}_{z,i,j,k+1/2} - F^{**}_{z,i,j,k-1/2}}{\Delta z} - C^n_{i,j,k}\frac{w_{i,j,k+1/2} - w_{i,j,k-1/2}}{\Delta z}\Delta t, \tag{17}$$

where $F_{x,i+1/2,j,k}$, $F_{y,i,j+1/2,k}$, $F_{z,i,j,k+1/2}$ are expressed as followss

$$F_{x,i+1/2,j,k} = -\frac{1}{\Delta y\Delta z}\int_{z_{i,j,k-1/2}}^{z_{i,j,k+1/2}}\int_{y_{i,j-1/2,k}}^{y_{i,j+1/2,k}}\int_{x_{i+1/2,j,k}}^{x_{i+1/2,j,k}-u_{i+1/2,j,k}\Delta t}\chi_{is,j,k}(x,y,z)dxdydz, \tag{18}$$

$$F_{y,i,j+1/2,k} = -\frac{1}{\Delta x\Delta z}\int_{z_{i,j,k-1/2}}^{z_{i,j,k+1/2}}\int_{y_{i,j+1/2,k}}^{y_{i,j+1/2,k}-v_{i,j+1/2,k}\Delta t}\int_{x_{i-1/2,j,k}}^{x_{i+1/2,j,k}}\chi_{i,js,k}(x,y,z)dxdydz, \tag{19}$$

$$F_{z,i,j,k+1/2} = -\frac{1}{\Delta x\Delta y}\int_{z_{i,j,k+1/2}}^{z_{i,j,k+1/2}-w_{i,j,k+1/2}\Delta t}\int_{y_{i,j-1/2,k}}^{y_{i,j+1/2,k}}\int_{x_{i-1/2,j,k}}^{x_{i+1/2,j,k}}\chi_{i,j,ks}(x,y,z)dxdydz. \tag{20}$$

Here, $F_{x,i+1/2,j,k}$, $F_{y,i,j+1/2,k}$ and $F_{z,i,j,k+1/2}$ are the advection fluxes for the x direction, y direction, and z direction, respectively. It is noted that subscripts *is, js* and *ks* are

$$is = \begin{cases} i; & \text{if } u_{i+1/2,j,k} \geq 0; \\ i+1; & \text{if } u_{i+1/2,j,k} < 0, \end{cases} \tag{21}$$

$$js = \begin{cases} j; & \text{if } v_{i,j+1/2,k} \geq 0; \\ j+1; & \text{if } v_{i,j+1/2,k} < 0, \end{cases} \tag{22}$$

and

$$ks = \begin{cases} k; & \text{if } w_{i,j,k+1/2} \geq 0; \\ k+1; & \text{if } w_{i,j,k+1/2} < 0. \end{cases} \tag{23}$$

Because of the discontinuous character of the fraction function C, the Eq. (14) cannot be directly solved using C concept, so it is necessary to use flux expressions $F_{x,i+1/2,j,k}$, $F_{y,i,j+1/2,k}$ and $F_{z,i,j,k+1/2}$. In the level set method, the distance function ϕ is continuous and its advection equation is solved directly. This is how VOF methods and LS methods are different. The VOF flux terms are calculated by applying the tangent of hyperbola for interface capturing (THINC) [60–62] scheme with the weighed linear interface calculation (WLIC) introduced in Section 3.2.

2.3. Coupled volume of fluid and level set (CLSVOF) method

For a better mass conservation and an accurate calculation of surface normals in THINC/WLIC scheme, we are motivated to combine the LS and VOF method. The proposed CLSVOF method advects the level set function ϕ and the volume fraction C by solving their governing equations from t^n to t^{n+1}. Following the advection of ϕ and C, interface reconstruction is needed so that the two interfaces predictred by ϕ and C are close to each other.

An intermediate function $\eta = 2C^{n+1} - 1$ is introduced in the reconstruction procedure. The position of the interface is described by the isoline $\eta = 0$, which is the same as that indicated by $C^{n+1} = \frac{1}{2}$. In other words, the choice of the η function initially follows the sign of the C function to represent different fluids. However, η is a discontinuous function. To obtain the continuous distance function near $\eta = 0$, we iteratively solve the following equation until η reaches its steady-state solution near the interface

$$\frac{\partial \eta}{\partial \hat{\tau}} + \bar{S}(\eta_0)(|\nabla \eta| - 1) = 0, \tag{24}$$

where η_0 is intermediate level set function calculated at $\hat{\tau} = 0$. Following this, another intermediate level set function $\phi^{n+1,*}$ is constructed to ensure that it describes the same interface as C^{n+1},

$$\phi^{n+1,*} = \begin{cases} \eta, & \text{if } |\phi^{n+1}| \le \varepsilon, \\ \phi^{n+1}, & \text{if } |\phi^{n+1}| > \varepsilon. \end{cases} \tag{25}$$

From Eq. (25) we can tell that discontinuities appear at $|\phi^{n+1,*}| = \varepsilon$. To eliminate the discontinuity at $|\phi^{n+1,*}| = \varepsilon$, we iteratively solve the following equation until it reaches a steady state solution,

$$\frac{\partial \phi^{n+1,*}}{\partial \bar{\tau}} + \bar{S}(\phi_0^{n+1,*})(|\nabla \phi^{n+1,*}| - 1) = \lambda \delta(\phi^{n+1,*})|\nabla \phi^{n+1,*}|, \tag{26}$$

where $\phi_0^{n+1,*}$ is set as $\phi^{n+1,*}$ in Eq. (25). That is, the solution to Eq. (25) is used as the initial condition for Eq. (26). After a steady-state solution is reached, $\phi^{n+1,*}$ is the continuous distance function that describes the same interface as C^{n+1}. Reconstruction of the level set function from volume fraction is described above, including the initialization Eq. (24) and reinitialization Eq. (26). In the present study, reconstruction is conducted every 10 steps.

2.4. Integrating Navier-Stokes equations with volume of fluid functions

In the simulation of two-phase flow of gas and fluid with CLSVOF method, the three-dimensional Navier-Stokes equation is modified to include density and viscosity terms. The Navier-Stokes equation is written as follows:

$$\nabla \cdot \mathbf{u} = 0, \tag{27}$$

and

$$\frac{\partial \mathbf{u}}{\partial t} + (\mathbf{u} \cdot \nabla)\mathbf{u} = -\frac{\nabla p}{\rho(C)} + \frac{\nabla \cdot (2\mu(C)\mathbf{D})}{\rho(C)} + \mathbf{F}, \tag{28}$$

where $\mathbf{u} = (u, v, w)$ is the fluid velocity, p is the pressure field, $\mathbf{D} = \frac{1}{2}((\nabla \mathbf{u}) + (\nabla \mathbf{u})^T)$ is the strain tensor, and $\mathbf{F} = (0, 0, -g)$ is the gravitational force. $\rho(C)$ and $\mu(C)$ are density and viscosity, respectively. Note that C indicates the fraction function (or volume of fluid function).

Nondimensionalization analysis is a widely-used technique in fluid mechanics for convenience. The following four characteristic scales are adopted: L, U, $\Gamma = \frac{1}{2}\rho U^2$, $T = \frac{L}{U}$, where L is the characteristic length, U is the characteristic velocity, Γ is the characteristic pressure and T is the characteristic time. Using the above characteristic scales to nondimensionalize the variables in the mass continuity equation and momentum continuity equation, one can derive the following nondimensionalized variables:

$$\begin{gathered} x = x^* L,\ y = y^* L,\ z = z^* L,\ t = t^* T = t^*(L/U),\ \rho = \rho^* \rho_L \\ u = u^* U,\ v = v^* U,\ w = w^* U,\ p = p^* \Gamma = p^*(\rho_L U^2),\ \mu = \mu^* \rho_L \end{gathered} \tag{29}$$

We non-dimensionalize the governing equations using the chain rule, and leave out the symbol * on the upper right corner of the dimensionless variables. Eq. (28) can be rewritten as:

$$\frac{\partial \mathbf{u}}{\partial t} + (\mathbf{u} \cdot \nabla)\mathbf{u} = -\frac{\nabla p}{\rho(C)} + \frac{1}{Re}\frac{\nabla \cdot (2\mu(C)\mathbf{D})}{\rho(C)} + \frac{1}{Fr^2}\hat{\mathbf{e}}_g, \tag{30}$$

where nondimensionalized density ρ and viscosity μ are shown in the following equations respectively,

$$\begin{aligned} \rho &= C + \left(\frac{\rho_G}{\rho_L}\right)(1 - C), \\ \mu &= C + \left(\frac{\mu_G}{\mu_L}\right)(1 - C). \end{aligned} \tag{31}$$

The subscripts '*G*' and '*L*' in Eq. (31) represent gas and liquid phases, respectively. Two dimensionless parameters are obtained including Reynolds number *Re* representing ratio of the inertial force to viscous force of the fluid, and Froude number *Fr* representing ratio of the inertial force to gravity of the fluid. The two parameters are defined as below:

$$Re = \frac{\rho_L L U}{\mu_L}, Fr = \frac{U}{\sqrt{gL}}. \tag{32}$$

3. Numerical scheme

This study is presented to describe the interface for VOF equation and a CLSVOF algorithm which makes sure that LS function is correctly connected to the identical geometry described by VOF function. Advection of VOF is solved under the framework of THINC/WLIC, and LS is solved directly from its advection equation by the OCRWENO scheme. The IB method will be implemented for the evaluation of momentum forcing term, which adopts the volume fraction of solid on the body surface. Fig. 1 presents a detailed flowchart for the procedure of solving Navier-Stokes equations and CLSVOF/IB method.

3.1. Level set method solver

In the present calculation, the convection term in level set advection and re-initialization equations are discretized based on the optimized compact reconstruction weighted essentially non-oscillatory (OCRWENO) scheme [63] and weighted essentially non-oscillatory (WENO) [64] schemes, respectively. The OCRWENO scheme means that optimized coefficients can be derived by using the dispersion-relation preserving finite difference approximation to the first derivative $\frac{\partial \phi}{\partial x}$ in wavenumber space [63]. In WENO schemes, adaptive stencils are used to obtain high order accuracy and non-oscillatory performance near discontinuities at the same time. The third-order total variation diminishing Runge-Kutta (TVD-RK3) [65] is used in time advancement for level set advection and re-initialization equations.

3.1.1. Approximation of spatial derivatives in level set evolution equation

To reduce absolute truncation errors, obtain higher-order accuracy with less dispersion errors in smooth regions and to simultaneously avoid occurring discontinuous solutions near discontinuities, the OCRWENO scheme for the convective flux term in the level set evolution equation is applied. Consider one-dimensional case for example. The numerical fluxes $\hat{F}_{i+1/2}$ constructed from its neighbor values of *F*, can be calculated through the following tridiagonal matrix equation

$$\begin{aligned}&\left[\frac{2\omega_1+\omega_2}{3}\right]\hat{F}^L_{i-\frac{1}{2}} + \left[\frac{\omega_1+2(\omega_2+\omega_3)}{3}\right]\hat{F}^L_{i+\frac{1}{2}} + \frac{\omega_3}{3}\hat{F}^L_{i+\frac{3}{2}}\\ &= \frac{\omega_1}{6}F_{i-1} + \left[\frac{5(\omega_1+\omega_2)+\omega_3}{6}\right]F_i + \left[\frac{\omega_2+5\omega_3}{6}\right]F_{i+1}.\end{aligned} \tag{33}$$

The non-constant weighting factors $\omega_k, k = 1, 2, 3$ in Eq. (33) are defined as

$$\omega_k = \frac{\alpha_k}{\sum_k \alpha_k}, \quad k = 1, 2, 3, \tag{34}$$

where

$$\alpha_k = c_k\left(1 + \frac{|\beta_1 - \beta_3|}{\beta_k + \epsilon}\right), \quad k = 1, 2, 3, \tag{35}$$

with $c_1 = 0.20891$, $c_2 = 0.5$ and $c_3 = 29109$, which are derived in compact scheme [63]. ϵ is set as 10^{-8} to avoid the denominator becoming zero. The smoothness indicators which can detect the smoothness of the numerical flux on a stencil in the solution are given by

$$\begin{aligned}\beta_1 &= \frac{13}{12}(F_{i-2} - 2F_{i-1} + F_i)^2 + \frac{1}{4}(F_{i-2} - 4F_{i-1} + 3F_i)^2,\\ \beta_2 &= \frac{13}{12}(F_{i-1} - 2F_i + F_{i+1})^2 + \frac{1}{4}(F_{i-1} - F_{i+1})^2,\\ \beta_3 &= \frac{13}{12}(F_i - 2F_{i+1} + F_{i+2})^2 + \frac{1}{4}(3F_i - 4F_{i+1} + F_{i+2})^2.\end{aligned} \tag{36}$$

The superscript "*L*" in Eq. (33) indicates that the numerical fluxes at cell faces are calculated in a left-biased interpolation. The numerical fluxes in the right-biased interpolation are also given below

$$\begin{aligned}&\left[\frac{2\widetilde{\omega}_1+\widetilde{\omega}_2}{3}\right]\hat{F}^R_{i+\frac{3}{2}} + \left[\frac{\widetilde{\omega}_1+2(\widetilde{\omega}_2+\widetilde{\omega}_3)}{3}\right]\hat{F}^R_{i+\frac{1}{2}} + \frac{\widetilde{\omega}_3}{3}\hat{F}^R_{i-\frac{1}{2}}\\ &= \frac{\widetilde{\omega}_1}{6}F_{i+2} + \left[\frac{5(\widetilde{\omega}_1+\widetilde{\omega}_2)+\widetilde{\omega}_3}{6}\right]F_{i+1} + \left[\frac{\widetilde{\omega}_2+5\widetilde{\omega}_3}{6}\right]F_i,\end{aligned} \tag{37}$$

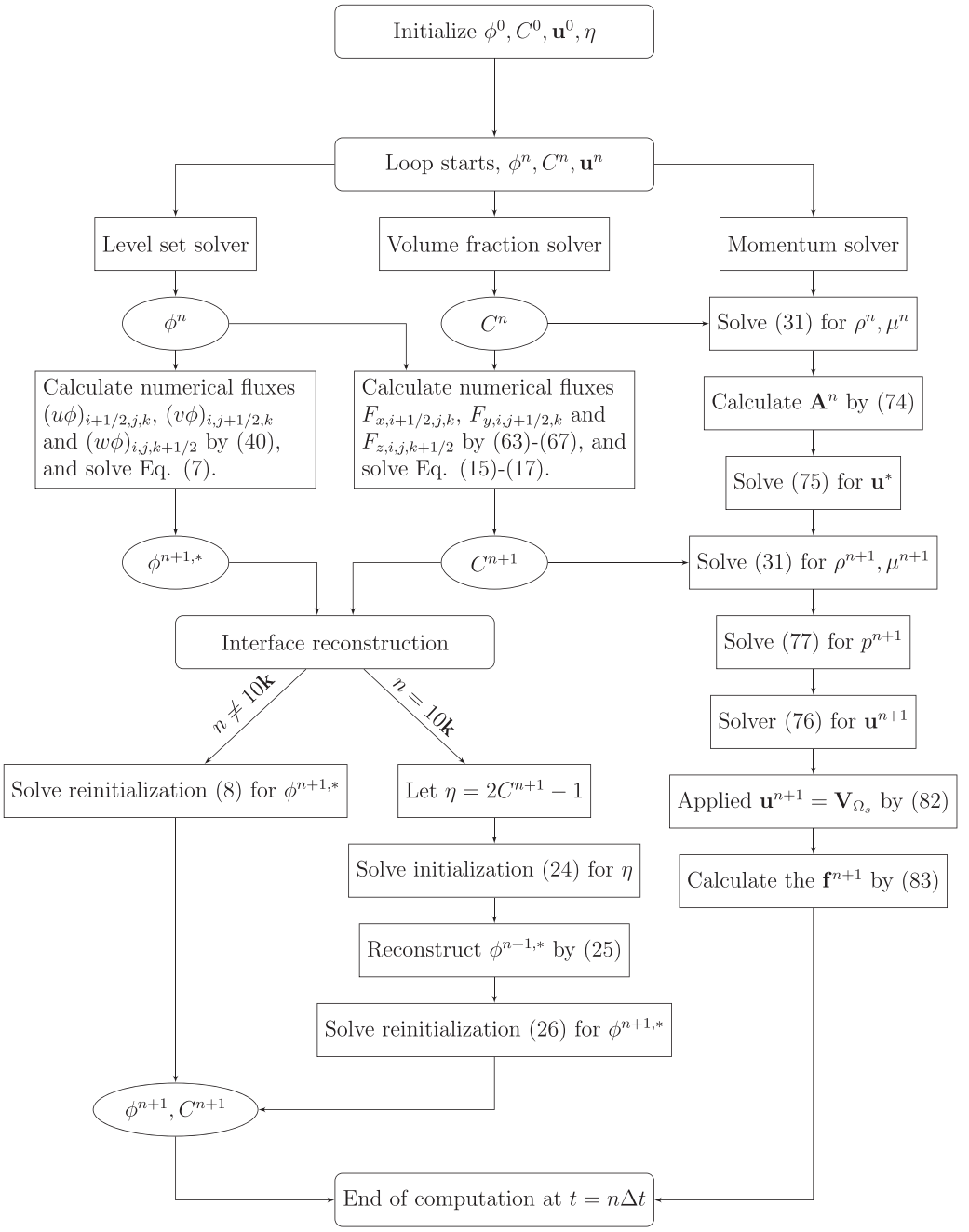

Fig. 1. Flow chart of the proposed solution algorithm, $\mathbf{k} \in \mathbb{N}$.

where

$$\widetilde{\omega}_k = \frac{\widetilde{\alpha}_k}{\sum_k \widetilde{\alpha}_k}, \ \widetilde{\alpha}_k = c_k\Big(1 + \frac{|\widetilde{\beta}_1 - \widetilde{\beta}_3|}{\widetilde{\beta}_k + \epsilon}\Big), \quad k = 1, 2, 3, \tag{38}$$

and

$$\widetilde{\beta}_1 = \frac{13}{12}(F_{i+1} - 2F_{i+2} + F_{i+3})^2 + \frac{1}{4}(F_{i+1} - 4F_{i+2} + 3F_{i+3})^2,$$
$$\widetilde{\beta}_2 = \frac{13}{12}(F_i - 2F_{i+1} + F_{i+2})^2 + \frac{1}{4}(F_i - F_{i+2})^2,$$

Table 1
The seven calculations performed in different grids and time-step sizes.

Section	Computational domain	Finest grids	Time-step size Δt
4.1	5×2.5	150×75	$\Delta t=0.01\Delta x$
4.2	$5\times 1\times 1.25$	$200\times 40\times 50$	$\Delta t=0.01\Delta x$
4.3	$10\times 1\times 1.2$	$400\times 40\times 48$	$\Delta t=0.01\Delta x$
5.1	$3.25\times 1\times 1$	$130\times 40\times 40$	$\Delta t=0.01\Delta x$
5.2	$16\times 6\times 7.5$	$160\times 60\times 75$	$\Delta t=0.01\Delta x$
5.3	$16\times 3.6\times 1$	$400\times 90\times 25$	$\Delta t=0.01\Delta x$
5.4	$16\times 5\times 7$	$240\times 75\times 105$	$\Delta t=0.01\Delta x$

Table 2
CPU time (recorded at $t=8$) for different periods of reconstruction of the problem of 2D dam-break flow.

Period (Steps)	CPU time (s)
5	303.3
10	298.43
15	265.19
20	243.65

Table 3
CPU time of different problems for different methods at different mesh sizes.

Method	Grids	CPU time(s)
Section 5.1, Dam-break flow with a short obstacle		
CLSVOF	$65\times 20\times 20$	1973
	$97\times 30\times 30$	6735
	$130\times 40\times 40$	18,244
LS	$130\times 40\times 40$	15,385
Section 5.2, Dam-break flow with a tall obstacle		
CLSVOF	$96\times 36\times 45$	2485
	$128\times 48\times 60$	6350
	$160\times 60\times 75$	15,493
LS	$160\times 60\times 75$	14,736
Section 5.3, Dam-break flow with a oblique obstacle		
CLSVOF	$320\times 72\times 20$	28,668
	$352\times 79\times 22$	36,659
	$400\times 90\times 25$	59,955
LS	$400\times 90\times 25$	53,718
Section 5.4, Dam-break flow with a cylinder obstacle		
CLSVOF	$160\times 50\times 70$	8581
	$192\times 60\times 84$	16,989
	$240\times 75\times 105$	40,615
LS	$240\times 75\times 105$	40,472

$$\widetilde{\beta}_3=\frac{13}{12}(F_{i-1}-2F_i+F_{i+1})^2+\frac{1}{4}(3F_{i-1}-4F_i+F_{i+1})^2. \tag{39}$$

Given the values of $F^L_{i+\frac{1}{2}}$ and $F^R_{i+\frac{1}{2}}$, numerical flux $F_{i+\frac{1}{2}}$ shown in Eq. (7) is calculated by using the flux splitting method

$$F_{i+\frac{1}{2}}=\left(u\phi\right)_{i+1/2}=\frac{1}{2}\left[\left(u^+\phi\right)^L_{i+1/2}+\left(u^-\phi\right)^R_{i+1/2}\right], \tag{40}$$

where $u^+=u+|u|$ and $u^-=u-|u|$. The boundary conditions are constructed using the WENO5 scheme and the detailed procedure can be found in Ref. [63]. The tridiagonal matrix algorithm (TDMA) method is used to efficiently solve the tridiagonal coefficient matrix.

3.1.2. Approximation of spatial derivatives for initialization equation

The semi-discrete form of the WENO scheme for the initialization equation can be expressed as [64]

$$\frac{\partial\phi}{\partial t}+H_G\left(\left(\frac{\partial\phi}{\partial x}\right)^+,\left(\frac{\partial\phi}{\partial x}\right)^-,\left(\frac{\partial\phi}{\partial y}\right)^+,\left(\frac{\partial\phi}{\partial y}\right)^-\right)=0, \tag{41}$$

where $(\frac{\partial\phi}{\partial x})^-_i$ (left-biased stencil from $i-3$ to $i+2$) and $(\frac{\partial\phi}{\partial x})^+_i$ (right-biased stencil from $i-2$ to $i+3$) in Eq. (41) are WENO approximations to $\frac{\partial\phi}{\partial x}(x_i,y_i)$, which are given by

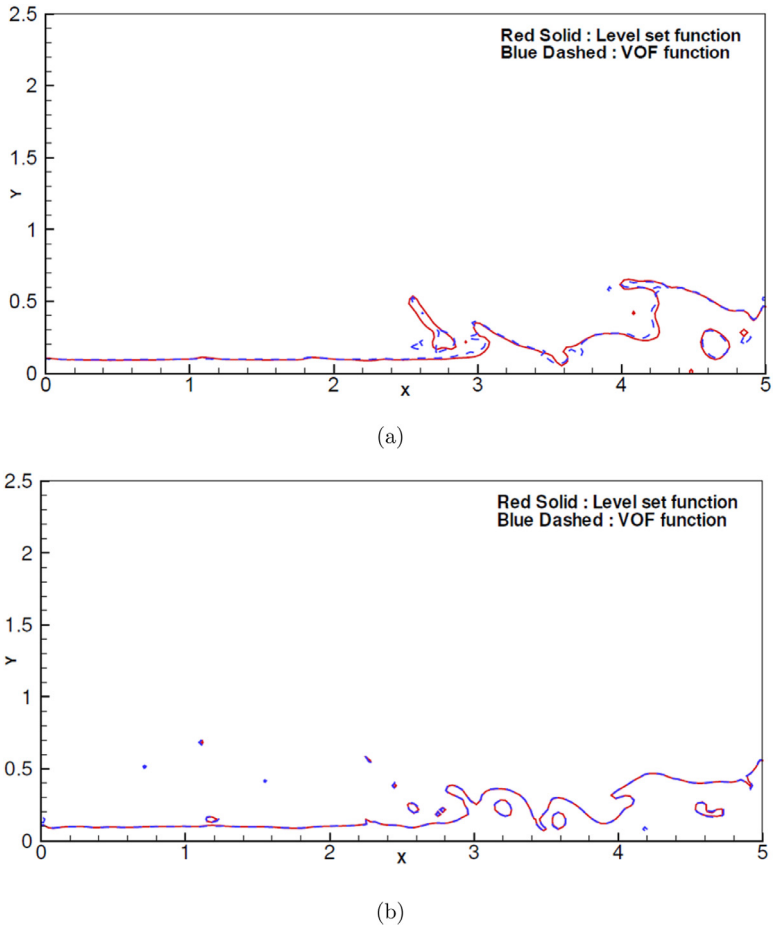

Fig. 2. Predicted interfaces 2D dam-break flow with dry bed for using mesh size $h = \frac{1}{30}$ and time step $\Delta t = 0.01h$ at $t = 8.0$. (a) Without the consideration of η function; (b) With the consideration of η function.

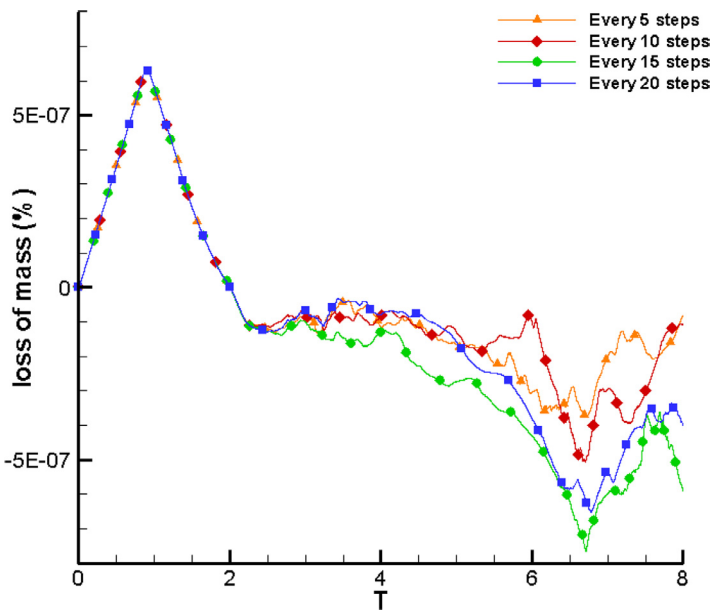

Fig. 3. Comparison of loss of mass for different periods of reconstruction for the problem of 2D dam-break flow.

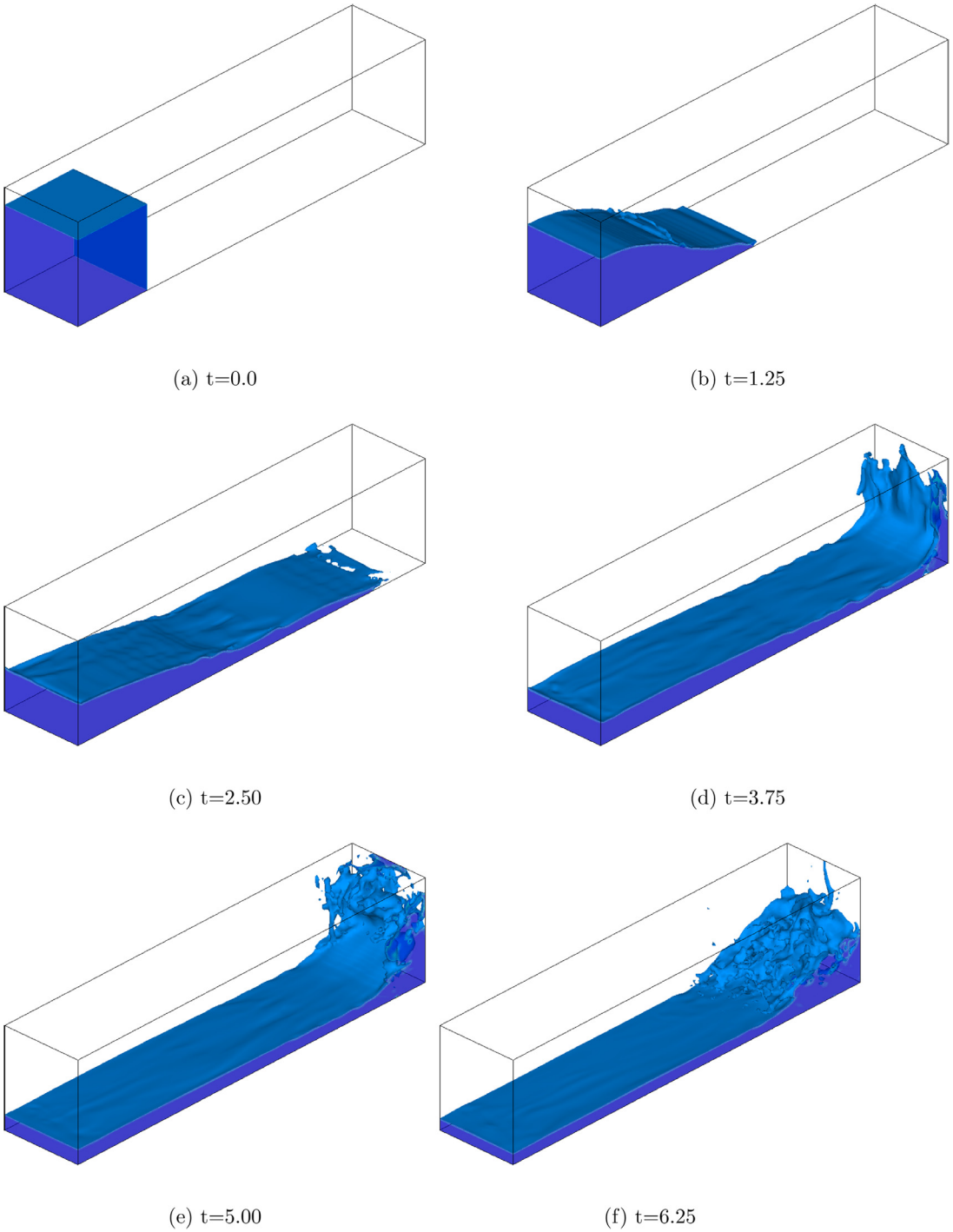

Fig. 4. Numerical results of dam-break flow with dry bed for **case A** using mesh size $h = \frac{1}{40}$ and time step $\Delta t = 0.01h$.

$$(\frac{\partial \phi}{\partial x})_i^- = \frac{1}{12}\left(-\frac{\triangle^+\phi_{i-2}}{\triangle x} + 7\frac{\triangle^+\phi_{i-1}}{\triangle x} + 7\frac{\triangle^+\phi_i}{\triangle x} - \frac{\triangle^+\phi_{i+1}}{\triangle x}\right)$$
$$-\phi^{WENO}\left(\frac{\triangle^-(\triangle^+\phi_{i-2})}{\triangle x}, \frac{\triangle^-(\triangle^+\phi_{i-1})}{\triangle x}, \frac{\triangle^-(\triangle^+\phi_i)}{\triangle x}, \frac{\triangle^-(\triangle^+\phi_{i+1})}{\triangle x}\right), \tag{42}$$

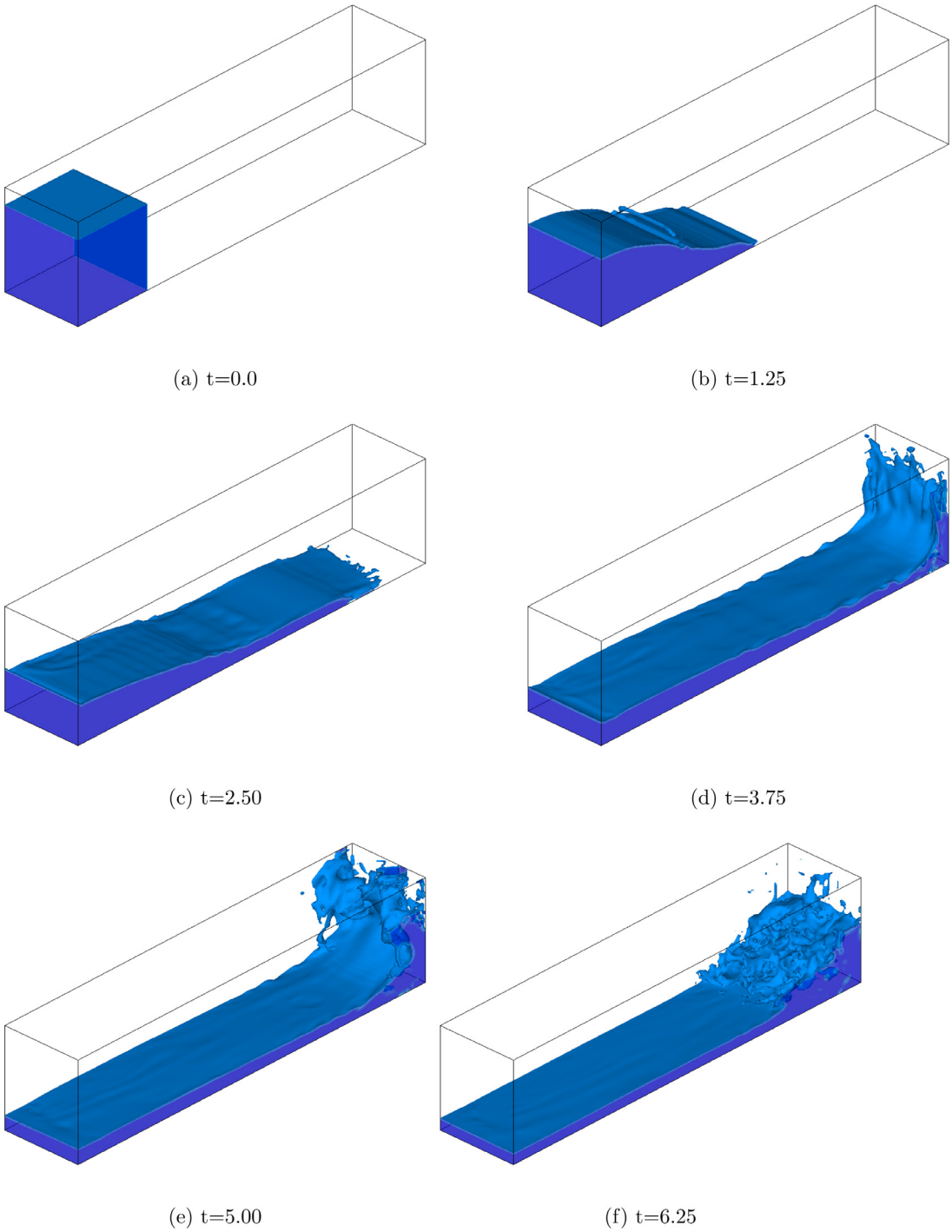

Fig. 5. Numerical results of dam-break flow with dry bed for **case B** using mesh size $h = \frac{1}{40}$ and time step $\Delta t = 0.01h$.

and

$$(\frac{\partial \phi}{\partial x})_i^+ = \frac{1}{12}\left(-\frac{\triangle^+\phi_{i-2}}{\triangle x} + 7\frac{\triangle^+\phi_{i-1}}{\triangle x} + 7\frac{\triangle^+\phi_i}{\triangle x} - \frac{\triangle^+\phi_{i+1}}{\triangle x}\right)$$
$$-\phi^{WENO}\left(\frac{\triangle^-(\triangle^+\phi_{i+2})}{\triangle x}, \frac{\triangle^-(\triangle^+\phi_{i+1})}{\triangle x}, \frac{\triangle^-(\triangle^+\phi_i)}{\triangle x}, \frac{\triangle^-(\triangle^+\phi_{i-1})}{\triangle x}\right). \quad (43)$$

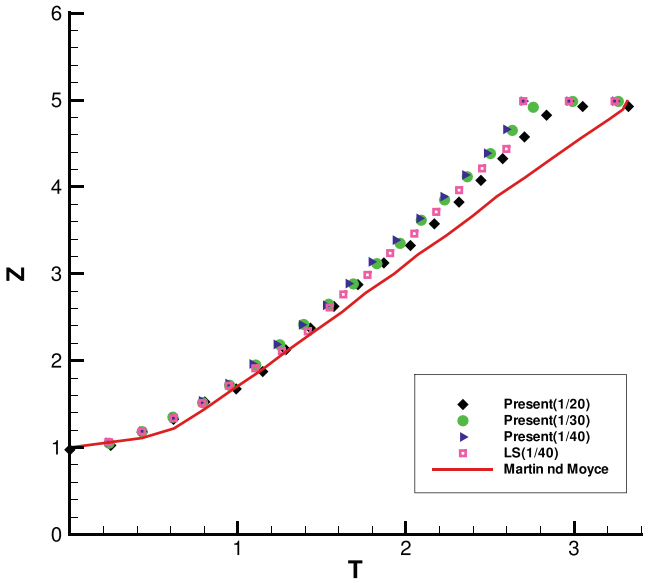

(a) Distance of surge front.

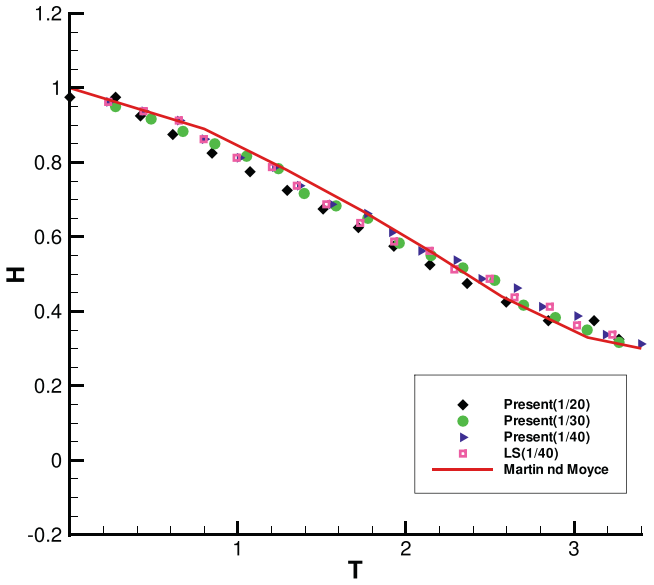

(b) Height of residual column.

Fig. 6. Comparison with experiment using three different mesh size with present method and level set method for **case A**.

In Eqs. (42) and (43), the notations $\triangle^+\phi_k = \phi_{k+1} - \phi_k$, $\triangle^-\phi_k = \phi_k - \phi_{k-1} (k = i-2 \sim i+2)$ are introduced. It should be noted that $\triangle^-(\triangle^+\phi_k)$ can be expressed to $\triangle^-(\triangle^+\phi_k) = \triangle^-(\phi_{k+1} - \phi_k) = \triangle^-\phi_{k+1} - \triangle^-\phi_k = (\phi_{k+1} - \phi_k) - (\phi_k - \phi_{k-1}) = \phi_{k+1} - 2\phi_k + \phi_{k-1}$. The obtained nonlinear function ϕ^{WENO} shown in Eqs. (42) and (43) can be expressed below in terms of **a, b, c, d**

$$\phi^{WENO}(\mathbf{a}, \mathbf{b}, \mathbf{c}, \mathbf{d}) = \frac{1}{3}\overline{\omega}_0(\mathbf{a} - 2\mathbf{b} + \mathbf{c}) + \frac{1}{6}\left(\overline{\omega}_2 - \frac{1}{2}\right)(\mathbf{b} - 2\mathbf{c} + \mathbf{d}), \tag{44}$$

with

$$\mathbf{a} = \frac{\triangle^-(\triangle^+\phi_{i-2})}{\triangle x}, \mathbf{b} = \frac{\triangle^-(\triangle^+\phi_{i-1})}{\triangle x}, \mathbf{c} = \frac{\triangle^-(\triangle^+\phi_i)}{\triangle x}, \mathbf{d} = \frac{\triangle^-(\triangle^+\phi_{i+1})}{\triangle x}, \tag{45}$$

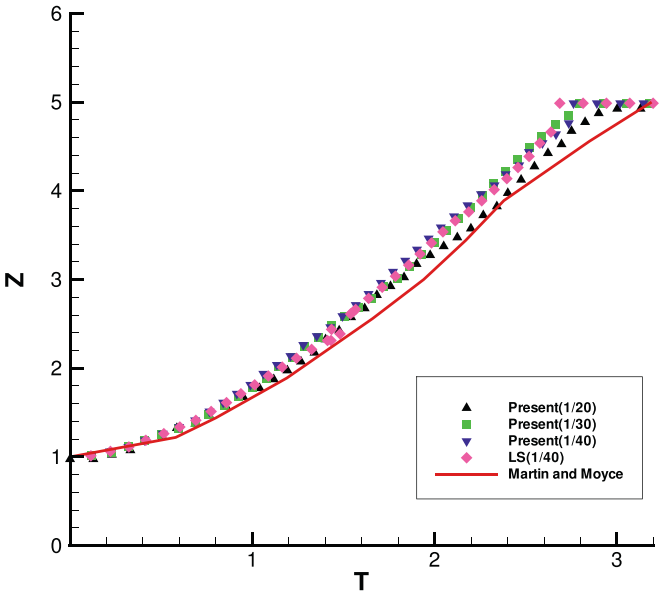

Fig. 7. Comparison with experiment using three different mesh size with present method and level set method for **case B**.

Table 4
Building corners' coordinates.

	x (m)	y (m)
Corner 1	3.44	−0.05
Corner 2	3.80	−0.23
Corner 3	4.15	0.49
Corner 4	3.79	0.67

Table 5
Gauge positions.

Gauge	x (m)	y (m)
G1	2.65	1.15
G2	2.65	−0.60
G4	4.00	−0.80
G6	−1.87	1.10

or

$$\mathbf{a} = \frac{\triangle^-(\triangle^+\phi_{i+2})}{\triangle x}, \mathbf{b} = \frac{\triangle^-(\triangle^+\phi_{i+1})}{\triangle x}, \mathbf{c} = \frac{\triangle^-(\triangle^+\phi_i)}{\triangle x}, \mathbf{d} = \frac{\triangle^-(\triangle^+\phi_{i-1})}{\triangle x}, \tag{46}$$

and weighting factors $\overline{\omega}_0$ and $\overline{\omega}_2$ in Eq. (44) are defined as

$$\overline{\omega}_0 = \frac{\overline{\alpha}_0}{\overline{\alpha}_0 + \overline{\alpha}_1 + \overline{\alpha}_2}, \overline{\omega}_2 = \frac{\overline{\alpha}_2}{\overline{\alpha}_0 + \overline{\alpha}_1 + \overline{\alpha}_2} \tag{47}$$

with

$$\overline{\alpha}_0 = \frac{1}{(\epsilon + IS_0)^2}, \overline{\alpha}_1 = \frac{6}{(\epsilon + IS_1)^2}, \overline{\alpha}_2 = \frac{3}{(\epsilon + IS_2)^2}, \tag{48}$$

and

$$\begin{aligned} IS_0 &= 13(\mathbf{a} - \mathbf{b})^2 + 3(\mathbf{a} - 3\mathbf{b})^2, \\ IS_1 &= 13(\mathbf{b} - \mathbf{c})^2 + 3(\mathbf{b} + \mathbf{c})^2, \\ IS_2 &= 13(\mathbf{c} - \mathbf{d})^2 + 3(3\mathbf{c} - \mathbf{d})^2. \end{aligned} \tag{49}$$

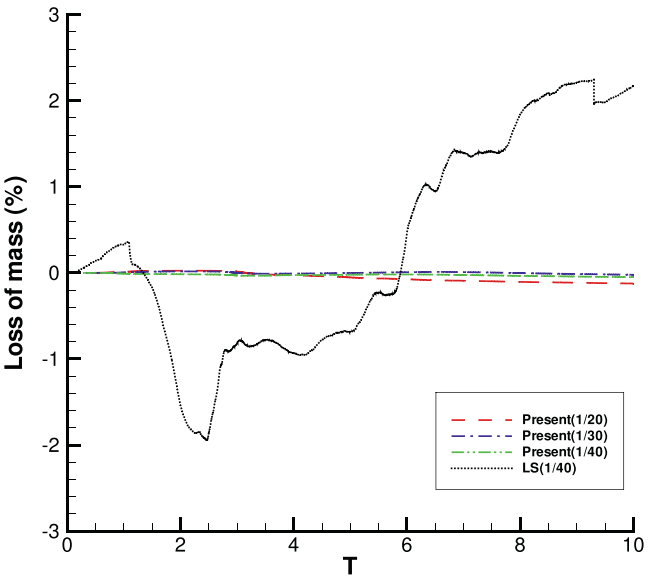

(a) Mass loss evolution.

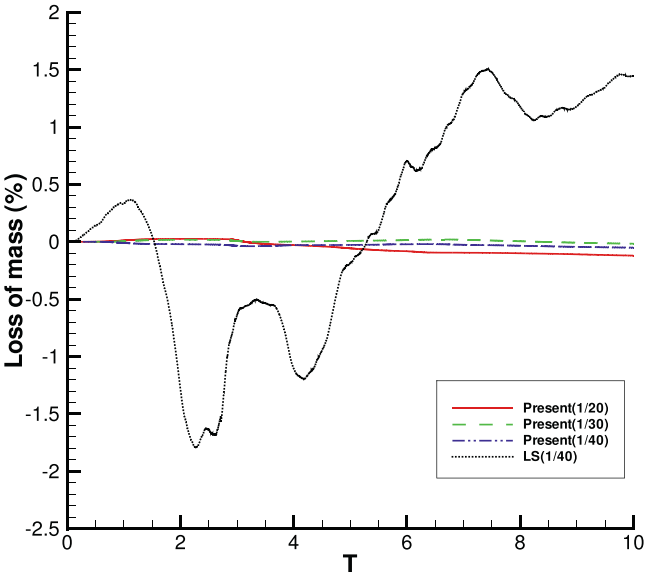

(b) Mass loss evolution.

Fig. 8. Mass loss evolution using present method and level set method (a) **case A**; (b) **case B**.

It is noted that ε is chosen to avoid division by zero according to the suggestion of Jiang and Shu [64]. We use the following Godunov flux H_G in Eq. (41) [65]

$$H_G(\bar{a},\bar{b},\bar{c},\bar{d}) = \begin{cases} \bar{S}(\phi_0)\left(\sqrt{[\mathbf{max}(\bar{a}^-,\bar{b}^+)]^2+[\mathbf{max}(\bar{c}^-,\bar{d}^+)]^2}-1\right); & if\phi_0 \geq 0, \\ \bar{S}(\phi_0)\left(\sqrt{[\mathbf{max}(\bar{a}^+,\bar{b}^-)]^2+[\mathbf{max}(\bar{c}^+,\bar{d}^-)]^2}-1\right); & otherwise, \end{cases} \tag{50}$$

where $\bar{a}^+ = \mathbf{max}(\bar{a},0)$ and $\bar{a}^- = \mathbf{min}(\bar{a},0)$.

3.1.3. Approximation of spatial derivatives for re-initialization equation

In fact, there are not significant improvements on dam-break flows simulated with shallow water equations spatially discretized with an order over 2. This study, however, focuses on capturing of the interface accurately, which requires higher

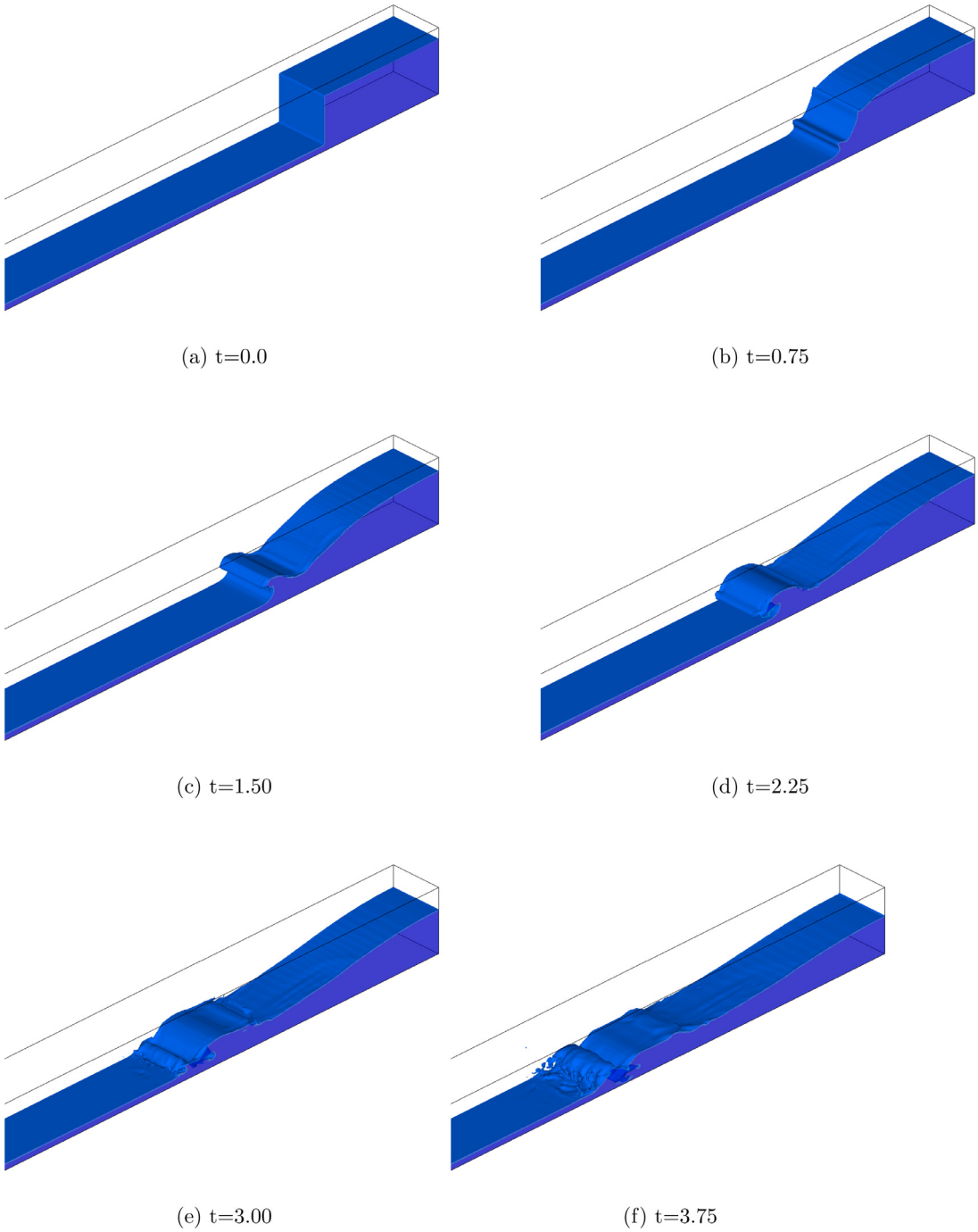

Fig. 9. Numerical results of dam-break flow with wet bed using present method with mesh size $h = \frac{1}{40}$ and time step $\Delta t = 0.01h$.

order schemes, so that mass is conserved as much as possible [63]. A fifth-order WENO scheme described in Section 3.1.2 is used for the spatial discretization of re-initialization equation (i.e. Eq. (8)). Since we only require that the level set function should be a distance function in the vicinity of the interface, it is not necessary to obtain a steady-state solution for Eq. (1) over the whole domain. A fixed number of iterations can be used to ensure the distance function property near the interface. For example, if the iteration step size is $\Delta\tau$, and the total interface thickness is 2ϵ, we can terminate the iteration process after no more than $\frac{\epsilon}{\Delta\tau}$ time steps. In practice it turns out that we need only three iterations since we are already close to the distance function. Re-initialization equation is also advanced in time with the TVD-RK3 scheme. The Courant-Friedrichs-Lewy (CFL) condition we have used include $\Delta t = \Delta x$, $\Delta t = 0.5\Delta x$ and $\Delta t = 0.25\Delta x$. We found that $\Delta t = 0.5\Delta x$

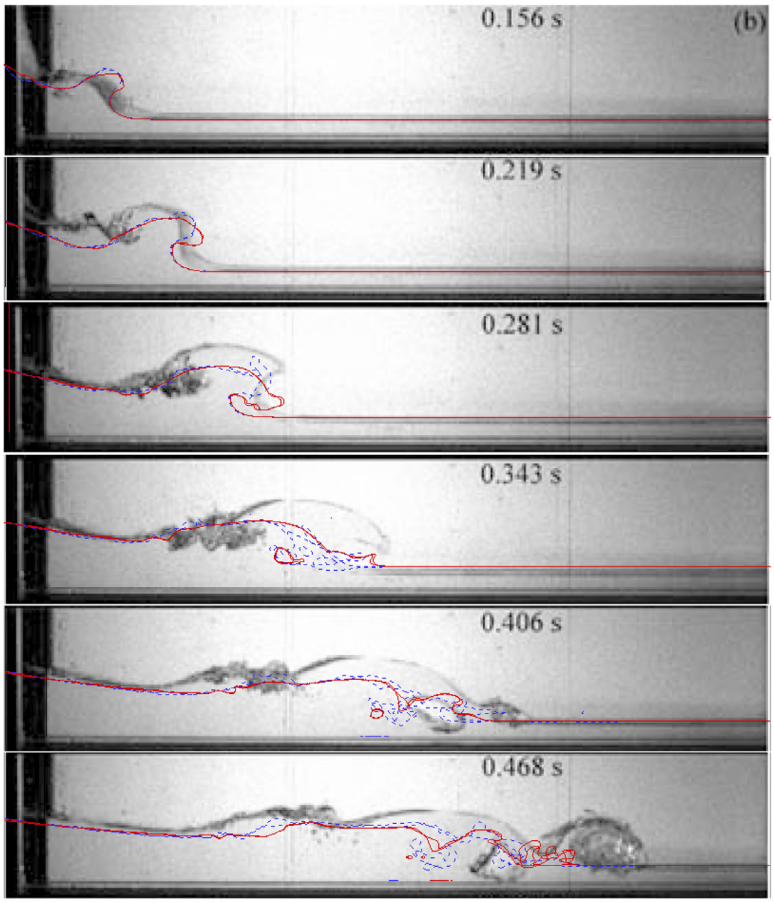

Fig. 10. Comparison to the experiments using present CLSVOF method (red) and the level set method (blue) with mesh size $h = \frac{1}{40}$ and time step $\Delta t = 0.01h$. (For interpretation of the references to colour in this figure legend, the reader is referred to the web version of this article.)

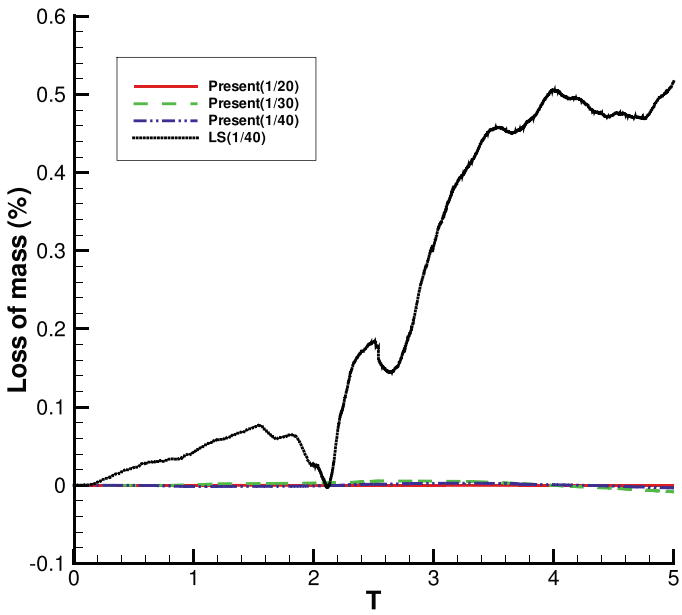

Fig. 11. Comparison of mass loss evolution for present CLSVOF method and level set method.

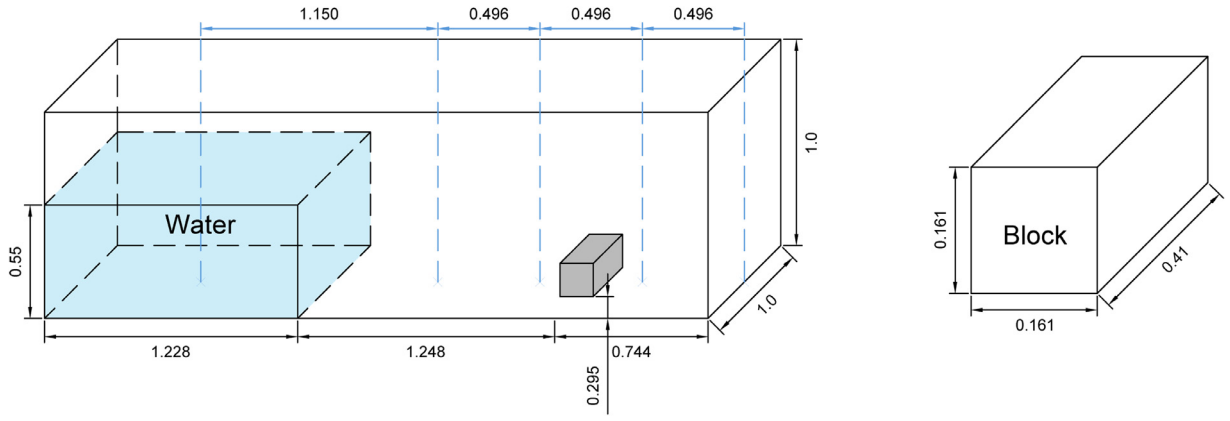

Fig. 12. The geometry of the tank together with placement of the obstacle.

is enough to avoid numerical instability. However, we still use CFL=0.25 (i.e. $\Delta t = 0.25\Delta x$) for Eq. (8) and indeed there is no numerical instability found for all cases with this CFL number.

3.2. Volume of fluid (VOF) solver

3.2.1. Weighed linear interface calculation (WLIC)

Following the idea of Simple Linear Interface Calculation (SLIC) method given in [13], Yokoi [59] defines an interface which is reconstructed from interfaces along three spatial directions with the weights. The weights are related to the local geometry of the interface, and are calculated from the surface normal $\mathbf{n}$

$$\chi_{i,j,k}(x,y,z) = \omega_{x,i,j,k}(\mathbf{n}_{i,j,k})\chi_{x,i,j,k}(x,y,z) + \omega_{y,i,j,k}(\mathbf{n}_{i,j,k})\chi_{y,i,j,k}(x,y,z) + \omega_{z,i,j,k}(\mathbf{n}_{i,j,k})\chi_{z,i,j,k}(x,y,z), \tag{51}$$

where $\chi_{x,i,j,k}(x,y,z)$, $\chi_{y,i,j,k}(x,y,z)$ and $\chi_{z,i,j,k}(x,y,z)$ are the characteristic functions along x, y and z directions, respectively. The weighting factors $\omega_{x,i,j,k}$, $\omega_{y,i,j,k}$ and $\omega_{z,i,j,k}$ can be obtained by calculating $n_{x,i,j,k}$, $n_{y,i,j,k}$, and $n_{z,i,j,k}$, which are the components of the surface normal $\mathbf{n}_{i,j,k}$ in x, y and z direction, respectively. The weighting factors are expressed as follows

$$\omega_{x,i,j,k} = \frac{|n_{x,i,j,k}|}{|n_{x,i,j,k}| + |n_{y,i,j,k}| + |n_{z,i,j,k}|}, \tag{52}$$

$$\omega_{y,i,j,k} = \frac{|n_{y,i,j,k}|}{|n_{x,i,j,k}| + |n_{y,i,j,k}| + |n_{z,i,j,k}|}. \tag{53}$$

and

$$\omega_{z,i,j,k} = \frac{|n_{z,i,j,k}|}{|n_{x,i,j,k}| + |n_{y,i,j,k}| + |n_{z,i,j,k}|}. \tag{54}$$

The surface normal near the interface can be calculated by using fraction function C [59]. It has been pointed out in [59] that the WLIC method is more accurate than classic VOF methods. However, due to the discontinuities across the interface, calculation of surface normal using VOF function may lead to numerical instability in the simulation. To overcome the drawback in the original WLIC scheme, the signed distance function, instead of VOF function, will be employed to calculate the value of surface normal. In the present CLSVOF method, surface normal can be expressed as follows

$$\mathbf{n}_{i,j,k} = \left.\frac{\nabla\phi}{|\nabla\phi|}\right|_{i,j,k}. \tag{55}$$

The gradient term $\nabla\phi$ shown in Eq. (55) is approximated by using the central difference scheme

$$(\nabla\phi)_{i,j,k} = \frac{\phi_{i+1,j,k} - \phi_{i-1,j,k}}{2\Delta x}\hat{x} + \frac{\phi_{i,j+1,k} - \phi_{i,j-1,k}}{2\Delta y}\hat{y} + \frac{\phi_{i,j,k+1} - \phi_{i,j,k-1}}{2\Delta z}\hat{z} \tag{56}$$

3.2.2. Tangent of hyperbola for interface capturing (THINC) scheme

A pure algebraic method without geometrical reconstruction has been proposed in [60], called THINC. In one-dimensional cases, the piecewise hyperbolic tangent function is employed as the characteristic function

$$\chi_{x,i} = \frac{1}{2}\left[1 + \alpha\tanh\left(\beta\left(\frac{x - x_{i-1/2}}{\Delta x} - \tilde{x}_i\right)\right)\right], \tag{57}$$

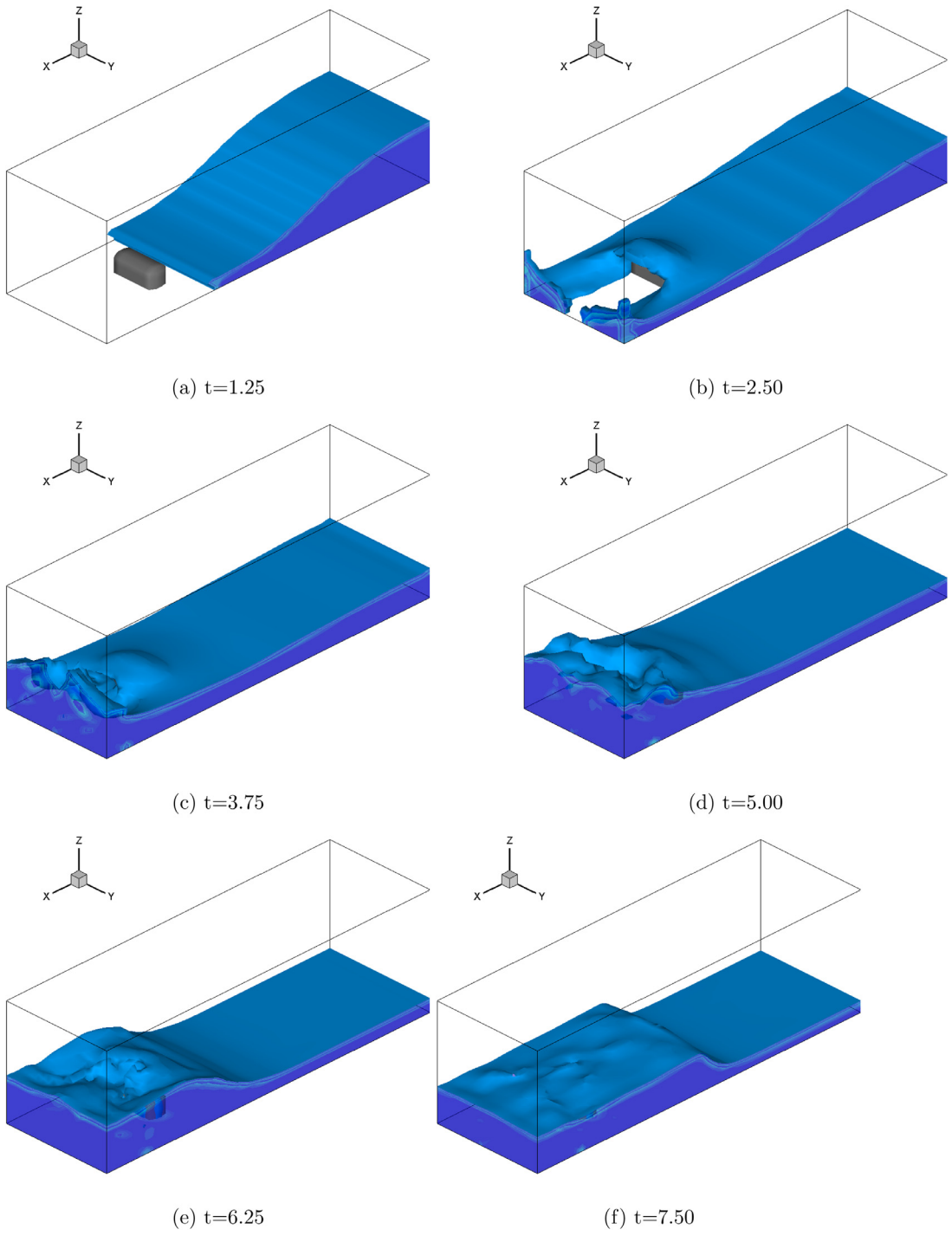

Fig. 13. Numerical results of dam-break flow with an obstacle solved by present method with mesh size $h = \frac{1}{20}$ and time step $\Delta t = 0.01h$.

where $\alpha = 1$ for $C_{i-1} < C_{i+1}$ and $\alpha = -1$ for $C_{i-1} > C_{i+1}$. β is a parameter introduced to control the slope and thickness of the jump, which is set as $\beta = 3.5$ in [60]. The jump center $\tilde{x}_i$ shown in Eq. (57) can be determined by the following equation

$$C_i = \frac{1}{\Delta x_i} \int_{x_{i-\frac{1}{2}}}^{x_{i+\frac{1}{2}}} \chi_{x,i}(x) dx$$

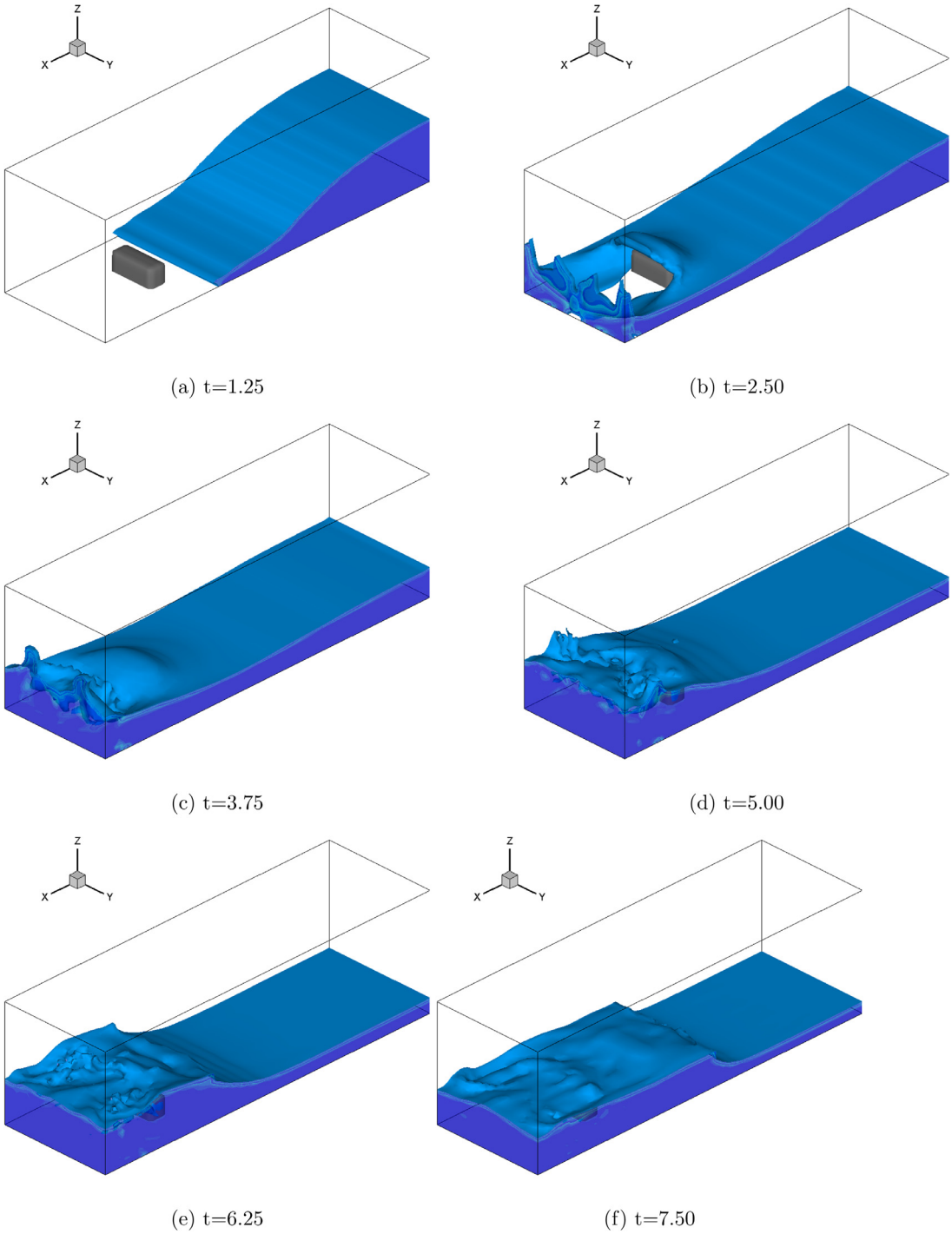

Fig. 14. Numerical results of dam-break flow with an obstacle solved by present method with mesh size $h = \frac{1}{30}$ and time step $\Delta t = 0.01h$.

$$= \frac{1}{\Delta x}\int_{x_{i-1/2}}^{x_{i+1/2}} \frac{1}{2}\left[1 + \alpha \tanh\left(\beta\left(\frac{x - x_{i-1/2}}{\Delta x} - \tilde{x}_i\right)\right)\right] dx. \tag{58}$$

An improved THINC scheme, called THINC of Slope Weighting (THINC/SW), with extreme simplicity yet considerable accuracy, has been further discussed in [61].

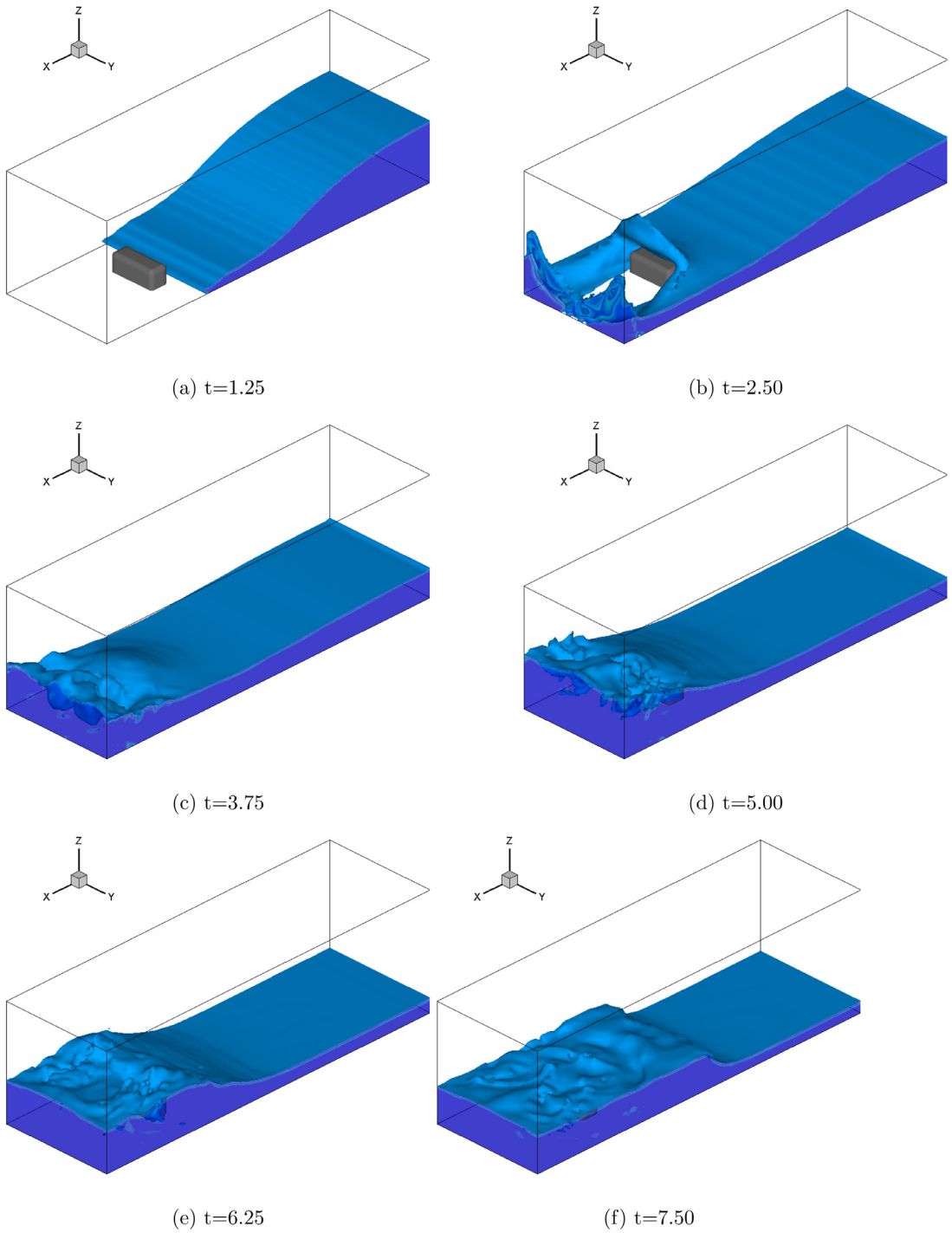

Fig. 15. Numerical results of dam-break flow with an obstacle solved by present method with mesh size $h = \frac{1}{40}$ and time step $\Delta t = 0.01h$.

3.2.3. THINC/WLIC scheme

The numerical flux $F_{x,i+1/2,j,k}$ shown in Eq. (15) can be calculated with an appropriate characteristic function $\chi_{i,j,k}(x, y, z)$ shown in Eq. (51)

$$\begin{aligned} F_{x,i+1/2,j,k} &= -\int_{z_{i,j,k-1/2}}^{z_{i,j,k+1/2}} \int_{y_{i,j-1/2,k}}^{y_{i,j+1/2,k}} \int_{x_{i+1/2,j,k}}^{x_{i+1/2,j,k}-u_{i+1/2,j,k}\Delta t} \chi_{is,j,k}(x, y, z)dxdydz, \\ &= F_{x,x,i+1/2,j,k} + F_{x,y,i+1/2,j,k} + F_{x,z,i+1/2,j,k} \end{aligned} \tag{59}$$

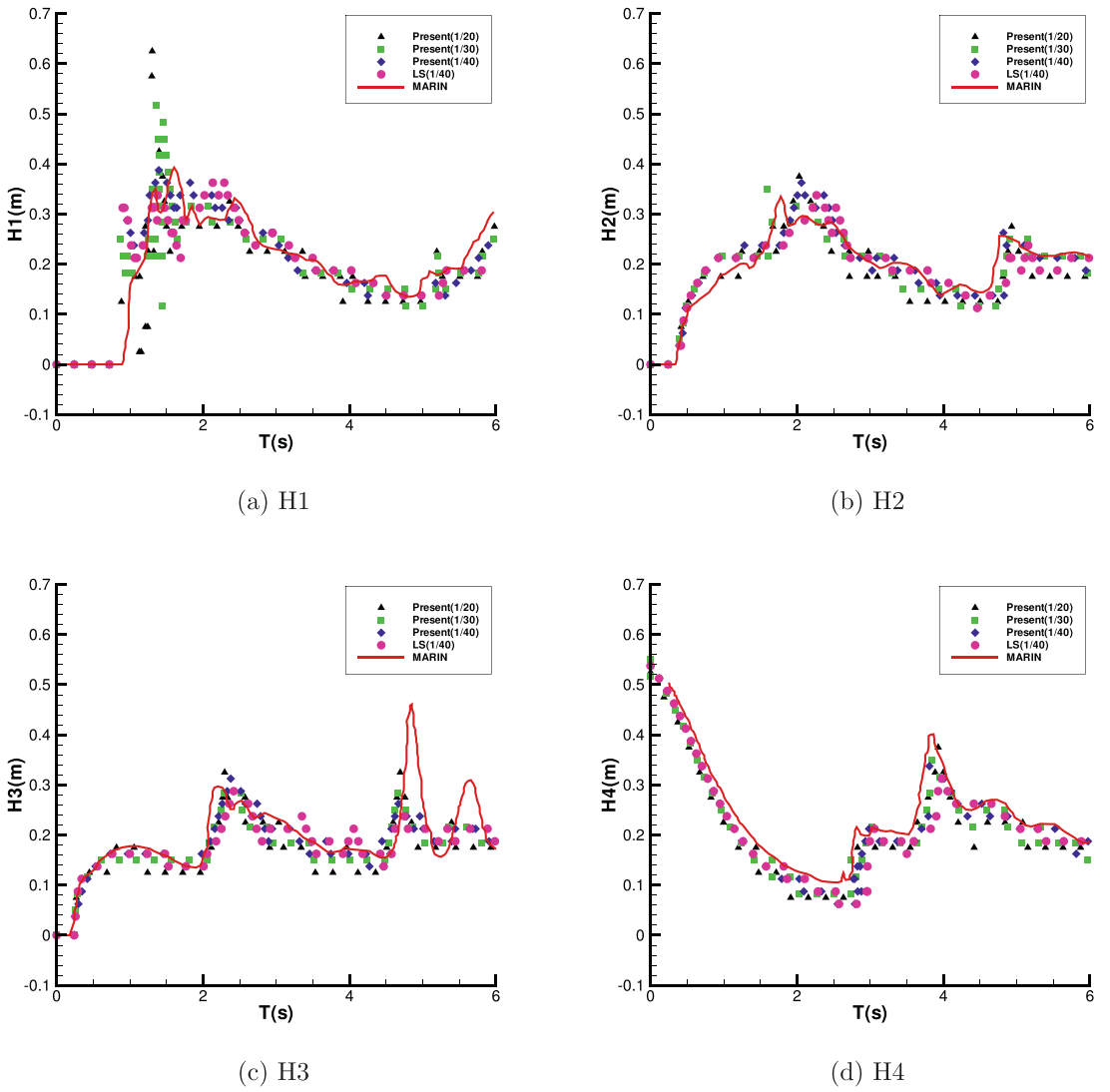

Fig. 16. Water levels at four distinct places for the dam-break flow with obstacle, comparison between numerical result and measured data. The result is carried out by present method with different mesh size.

where

$$F_{x,x,i+1/2,j,k} = -\frac{1}{\Delta y \Delta z}\int_{z_{i,j,k-1/2}}^{z_{i,j,k+1/2}}\int_{y_{i,j-1/2,k}}^{y_{i,j+1/2,k}}\int_{x_{i+1/2,j,k}}^{x_{i+1/2,j,k}-u_{i+1/2,j,k}\Delta t}\omega_{x,is,j,k}\chi_{x,is,j,k}dxdydz, \tag{60}$$

$$F_{x,y,i+1/2,j,k} = -\frac{1}{\Delta x \Delta z}\int_{z_{i,j,k-1/2}}^{z_{i,j,k+1/2}}\int_{y_{i,j-1/2,k}}^{y_{i,j+1/2,k}}\int_{x_{i+1/2,j,k}}^{x_{i+1/2,j,k}-u_{i+1/2,j,k}\Delta t}\omega_{y,is,j,k}\chi_{y,is,j,k}dxdydz, \tag{61}$$

and

$$F_{x,z,i+1/2,j,k} = -\frac{1}{\Delta x \Delta y}\int_{z_{i,j,k-1/2}}^{z_{i,j,k+1/2}}\int_{y_{i,j-1/2,k}}^{y_{i,j+1/2,k}}\int_{x_{i+1/2,j,k}}^{x_{i+1/2,j,k}-u_{i+1/2,j,k}\Delta t}\omega_{y,is,j,k}\chi_{y,is,j,k}dxdydz. \tag{62}$$

Computation of the numerical flux $F_{x,i+1/2,j,k}$ by THINC/WLIC scheme is given below for convenience:

1. Calculate the jump location of the cell $\tilde{x}_{is,j,k}$ by

$$\tilde{x}_{is,j,k} = \frac{1}{2\beta}\ln\left(\frac{a_3^2 - a_1 a_3}{a_1 a_3 - 1}\right), \tag{63}$$

where $a_1 = \mathbf{exp}(\frac{\beta}{\alpha}(2C_{is,j,k} - 1))$ and $a_3 \equiv \mathbf{exp}(\beta)$.

2. Calculate the numerical flux $F_{x,x,i+1/2,j,k}$ by using the piecewise hyperbolic tangent function given in Eq. (57)

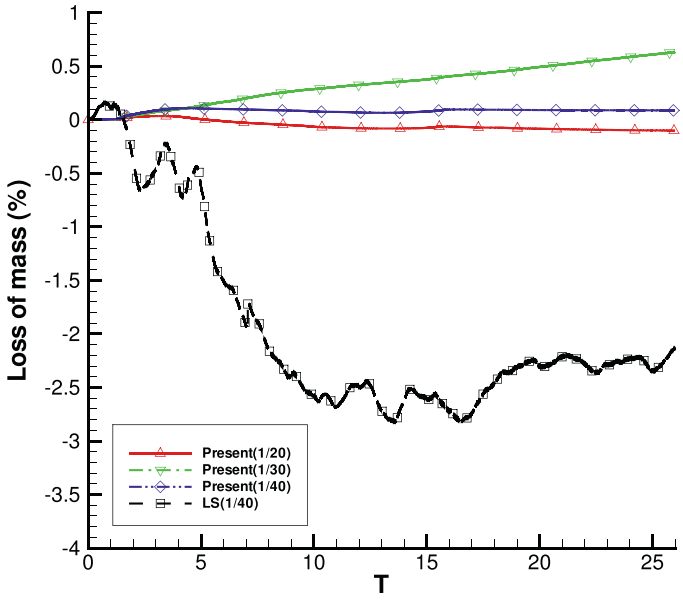

Fig. 17. Comparison of mass loss evolution using present method and level set method with different mesh size for the dam-break flow with obstacle.

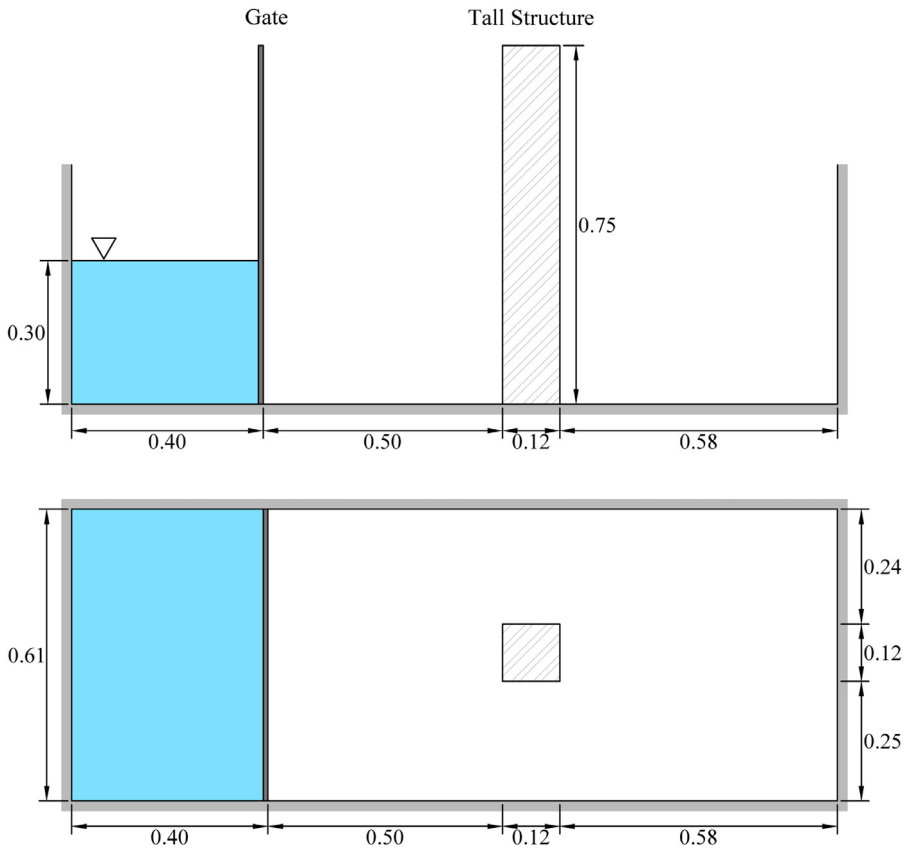

Fig. 18. Schematics of dam-break flow with a tall obstacle.

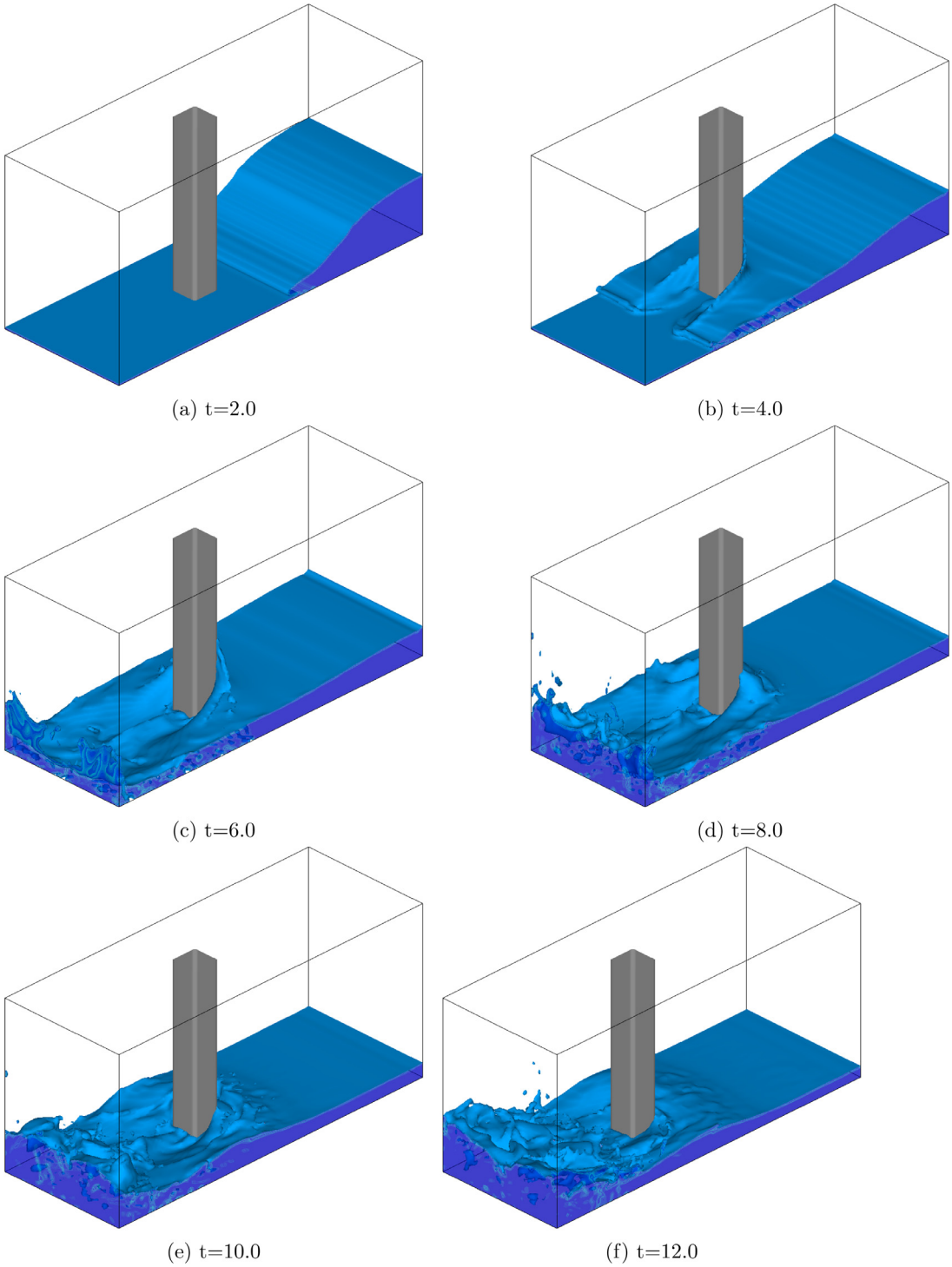

Fig. 19. Numerical results of dam-break flow over a tall obstacle solved by present method with mesh size $h = \frac{1}{10}$ and time step $\Delta t = 0.01h$.

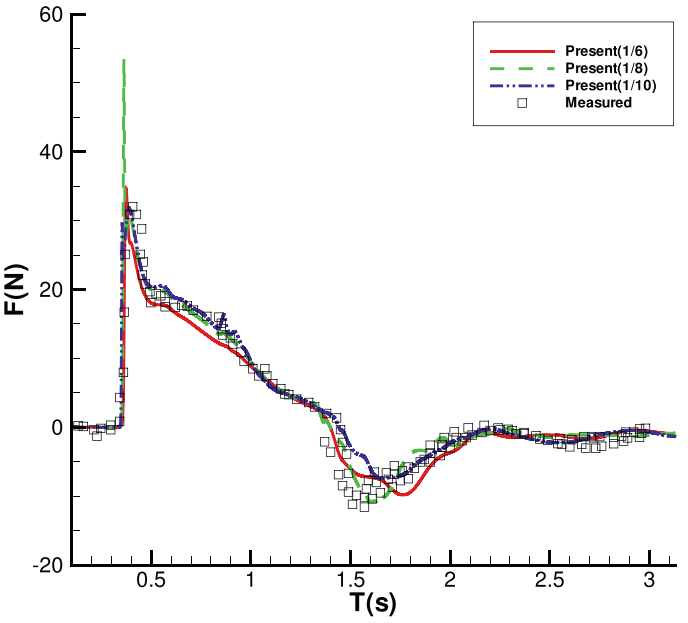

Fig. 20. Experimental and numerical column net force along x direction. The numerical result is obtained by present method using three different mesh size $\frac{1}{6}$, $\frac{1}{8}$ and $\frac{1}{10}$.

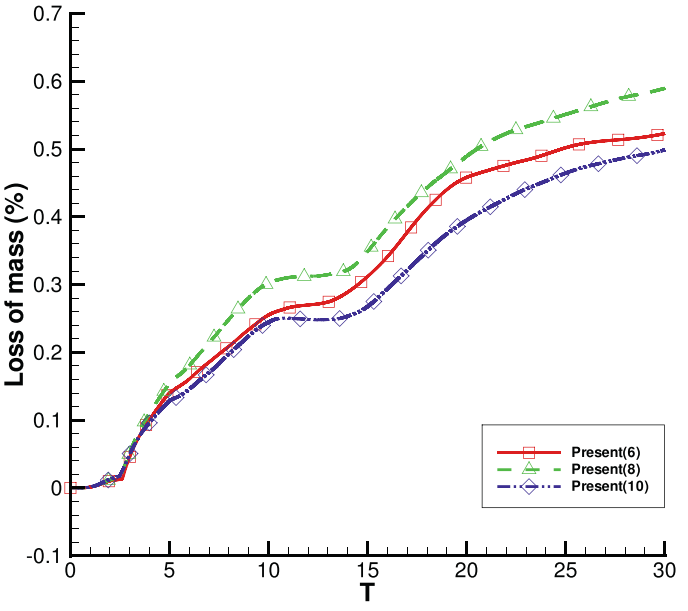

Fig. 21. Comparison of mass loss evolution for present method and level set method.

$$
\begin{aligned}
F_{x,x,i+1/2,j,k} &= -\frac{1}{\Delta y \Delta z}\int_{z_{i,j,k-1/2}}^{z_{i,j,k+1/2}}\int_{y_{i,j-1/2,k}}^{y_{i,j+1/2,k}}\int_{x_{i+1/2,j,k}}^{x_{i+1/2,j,k}-u_{i+1/2,j,k}\Delta t}\omega_{x,is,j,k}\chi_{x,is,j,k}dxdydz,\\
&= -\int_{x_{i+1/2,j,k}}^{x_{i+1/2,j,k}-u_{i+1/2,j,k}\Delta t}\frac{\omega_{x,is,j,k}}{2}\left[1+\alpha\tanh\left(\beta\left(\frac{x-x_{is-1/2,j,k}}{\Delta x}-\tilde{x}_{is,j,k}\right)\right)\right]dx,\\
&= -\frac{\omega_{x,is,j,k}}{2}\left[x+\frac{\alpha\Delta x}{\beta}\ln\left(\cosh\left(\beta\left(\frac{x-x_{is-1/2,j,k}}{\Delta x}\right)-\tilde{x}_{is,j,k}\right)\right)\right]_{x_{i+1/2,j,k}}^{x_{i+1/2,j,k}-u_{i+1/2,j,k}\Delta t},\\
&= \frac{\omega_{x,is,j,k}}{2}\left[u_{i+1/2,j,k}\Delta t-\frac{\alpha\Delta x}{\beta}\ln\left(\frac{a_4}{a_5}\right)\right],
\end{aligned}
\tag{64}
$$

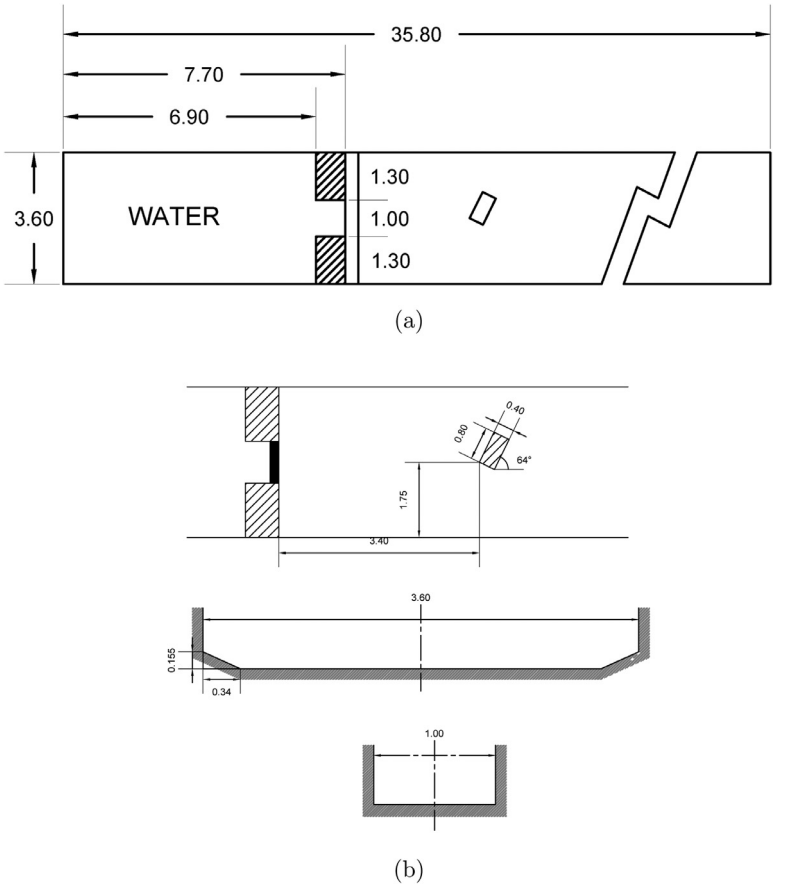

Fig. 22. (a) Dimensions of the channel and the oblique obstacle (*meter*). (b) Position of the oblique obstacle (upper), cross section in the channel and reservoir (middle) and at the dam (lower).

where $a_4 = \cosh[\beta(\gamma - u_{i+1/2,j,k}\frac{\Delta t}{\Delta x} - \tilde{x}_{is,j,k})]$, $a_5 = \cosh[\beta(\gamma - \tilde{x}_{is,j,k})]$. The value of γ is 1 if $u_{i+1/2,j,k} > 0$, and $\gamma = 0$ otherwise. The value of *is* is defined as

$$is = \begin{cases} i; & \text{if} \quad u_{i+1/2,j,k} \geq 0, \\ i+1; & \text{if} \quad u_{i+1/2,j,k} < 0. \end{cases} \tag{65}$$

3. Calculate the numerical flux $F_{x,\zeta,i+1/2,j,k} \equiv F_{x,y,i+1/2,j,k} + F_{x,z,i+1/2,j,k}$ by the following equation

$$F_{x,\zeta,i+1/2,j,k} = (1 - \omega_{x,is,j,k})C_{is,j,k}u_{i+1/2,j,k}\Delta t. \tag{66}$$

It is worthy addressing here that the weight $\omega_{x,is,j,k}$ is calculated by the level set function, as shown in Eq. (55).

4. Generalize the numerical flux term $F_{x,i+1/2,j,k}$ by adding $F_{x,x,i+1/2,j,k}$ and $F_{x,\zeta,i+1/2,j,k}$

$$F_{x,i+1/2,j,k} = F_{x,x,i+1/2,j,k} + F_{x,\zeta,i+1/2,j,k}. \tag{67}$$

One can refer to [59] for the calculation of the numerical fluxes $F_{y,i,j+1/2,k}$ and $F_{z,i,j,k+1/2}$.

3.3. Navier-Stokes equation solver

Discretization of the governing equations are carried out on a uniform staggered Cartesian grid. The velocity components *u, v*, and *w* are defined at centers of cell faces in the *x, y*, and *z* directions, respectively, while ρ, μ, p, ϕ and C are defined at cell centers.

3.3.1. Immersed boundary (IB) method

When fluid flows over a body, it can exert a force on the no-slip surface, and the surface will in return apply a force on the flow, which can bring the flow to rest on the body surface. This implies that the effect of the body in the flow can be

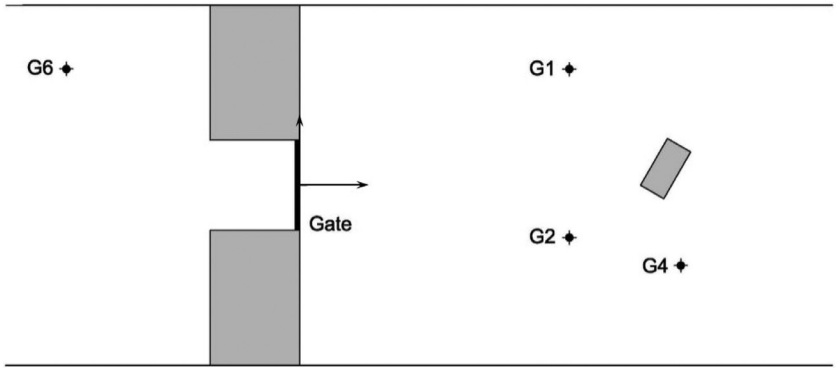

Fig. 23. Water level gauge positions.

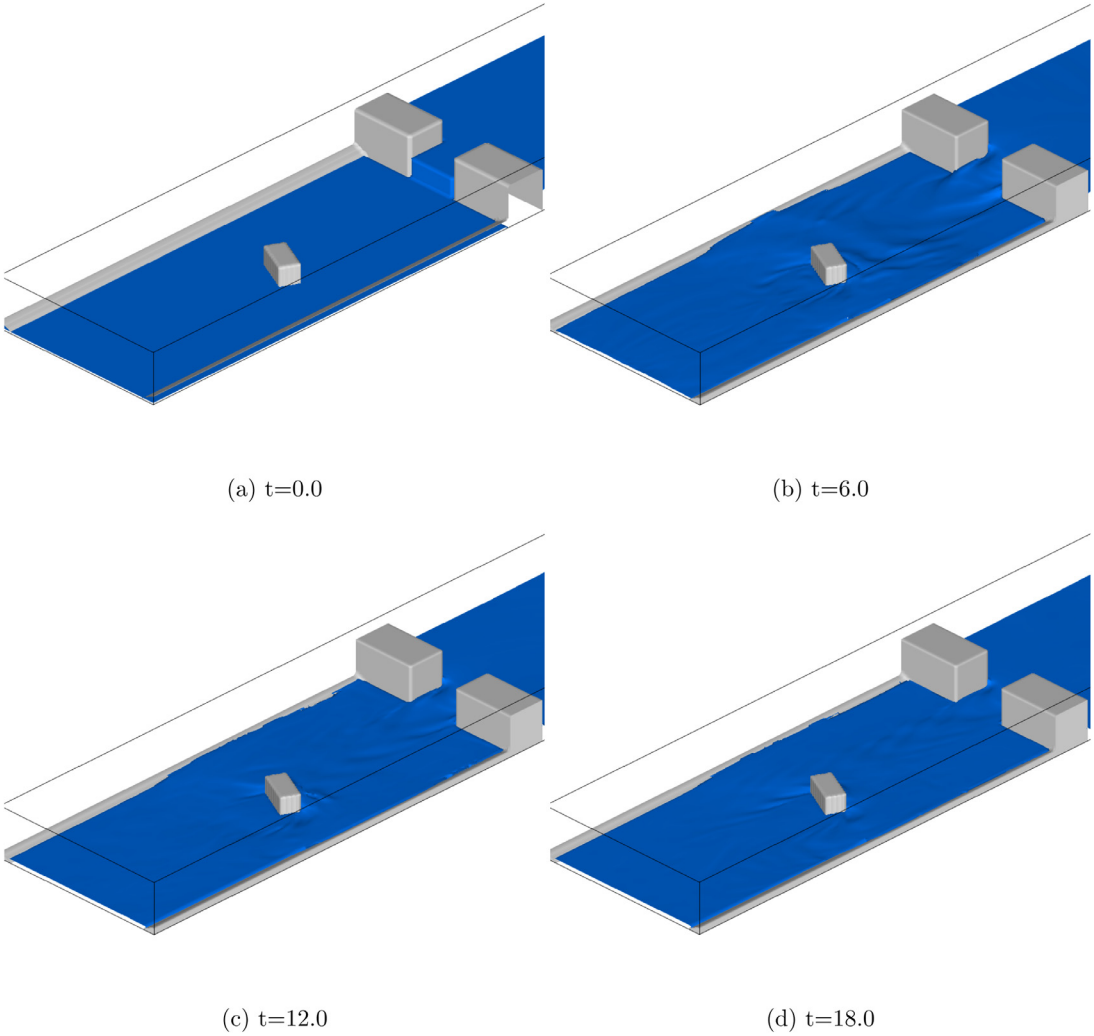

Fig. 24. Numerical results of dam-break flow over an oblique obstacle solved by present method with mesh size $h = \frac{1}{25}$ and time step $\Delta t = 0.01h$.

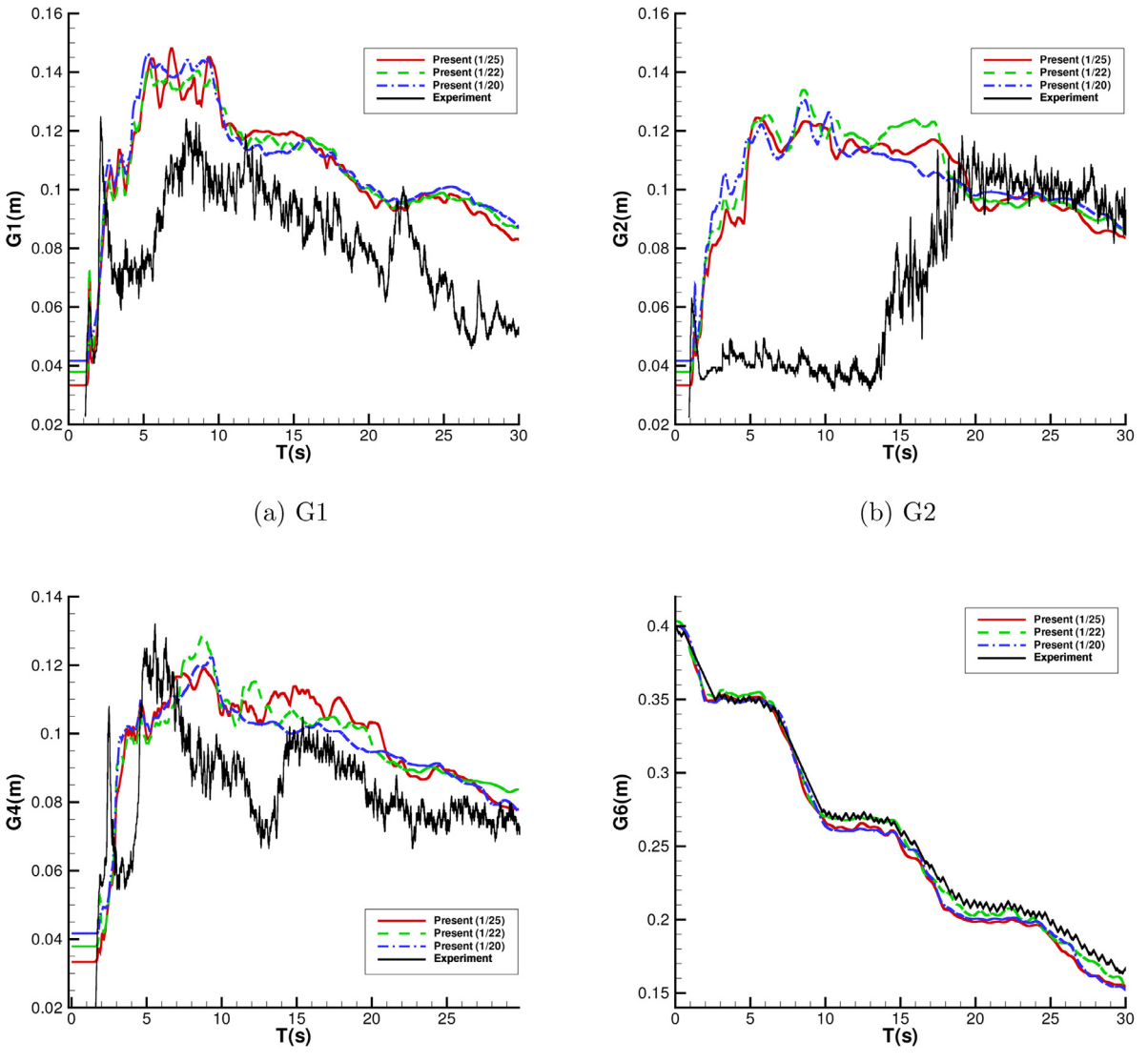

Fig. 25. Water level revolution at four distinct place using present method with three different mesh size, $\frac{1}{20}$, $\frac{1}{22}$ and $\frac{1}{25}$.

simulated by such a body force externally applied to the momentum equations at certain points in the flow. In this way, the IB method simulates complex bodies by introducing an artificial force to the momentum equations in the vicinity of the immersed boundary [53]. The resulting momentum equations can be written as

$$\frac{\partial \mathbf{u}}{\partial t} + (\mathbf{u}\cdot\nabla)\mathbf{u} = -\frac{\nabla p}{\rho(C)} + \frac{\nabla\cdot(2\mu(C)\mathbf{D})}{\rho(C)} + \mathbf{F} + \mathbf{f}_{IB}. \tag{68}$$

As indicated by the name of discrete-time momentum forcing method, the forcing vector $\mathbf{f}_{IB}$ in the above equation can be directly computed from the discrete-time momentum vector equation as follows

$$\begin{aligned} \tfrac{\mathbf{u}^{n+1}-\mathbf{u}^{n}}{\Delta t} &= -(\mathbf{u}\cdot\nabla)\mathbf{u} - \tfrac{\nabla p}{\rho(C)} + \tfrac{\nabla\cdot(2\mu(C)\mathbf{D})}{\rho(C)} + \mathbf{F} + \mathbf{f}_{IB} \\ &= \underline{RHS} + \mathbf{f}_{IB}. \end{aligned} \tag{69}$$

It is noted that the momentum forcing vector $\mathbf{f}_{IB}$ is applied on the immersed boundary. This ensures that the no-slip condition holds for the velocity along an arbitrary immersed boundary $\delta\Omega_s$. In other words, the force term $\mathbf{f}_{IB}$ can ensure that the magnitude of the velocity equals $\mathbf{V}_{\Omega_s}$. For cases where the immersed boundary is perfectly aligned with the grid, the magnitude of velocity on $\delta\Omega_s$ will be directly set as $\mathbf{V}_{\Omega_s}$. In practice, the immersed boundary can be more complex. Therefore, the interpolation of the momentum forcing term will be required to render the velocity with a magnitude ap-

proximately equal to $\mathbf{V}_{\Omega_s}$ at the immersed boundary. In general, the momentum forcing vector can be calculated by using following equation

$$\mathbf{f}_{IB} = -\underline{RHS} + \frac{\mathbf{V}_{\Omega_s} - \mathbf{u}^n}{\Delta t}, \text{ on } \delta\Omega_s. \tag{70}$$

In the above equation, Δt represents the time step and $\mathbf{V}_{\Omega_s}$ denotes the specified velocity along the immersed boundary. The vector RHS shown above consists of the pressure gradient, convection, and diffusion terms in the momentum equation. In the case of a stationary solid body where no-slip boundary conditions are prescribed, $\mathbf{V}_{\Omega_s}$ will be specified along the boundary.

In this study, the force that structure exerts on the fluid is denoted by a forcing vector $\eta\mathbf{f}$, where η is the solid volume fraction. The effect of the immersed boundary on flow is simulated by introducing the forcing vector as a source term to the momentum equation:

$$\frac{\partial \mathbf{u}}{\partial t} + (\mathbf{u}\cdot\nabla)\mathbf{u} = -\frac{\nabla p}{\rho(C)} + \frac{1}{Re}\frac{\nabla\cdot(2\mu(C)\mathbf{D})}{\rho(C)} + \frac{1}{Fr^2}\hat{\mathbf{e}}_g + \eta\mathbf{f}. \tag{71}$$

As fluid imposes force on solid, solid can also impose a reacting force on fluid. Therefore, this term needs to be computed when the grid is on the solid. The solid volume fraction is defined here. In three-dimensional space, the value of solid volume fraction $\eta_{i,j,k}$ can be calculated in finer grids. To show the calculation of $\eta_{i,j,k}$, we consider a computational cell at node (i, j, k). This cell is uniformly cut into $N_x \times N_y \times N_z$ pieces of smaller cells, with a volume equal to $\Delta x' \times \Delta y' \times \Delta z'$. The location of each smaller cell, denoted as $(x_{m,n,l}, y_{m,n,l}, z_{m,n,l})$, can be expressed as follows

$$\begin{aligned} x_{m,n,l} &= \frac{1}{2}\left(x_{i-1,j,k} + x_{i,j,k}\right) + m\Delta x', \\ y_{m,n,l} &= \frac{1}{2}\left(y_{i,j-1,k} + y_{i,j,k}\right) + n\Delta y', \\ z_{m,n,l} &= \frac{1}{2}\left(z_{i,j,k-1} + z_{i,j,k}\right) + l\Delta z', \end{aligned} \tag{72}$$

where $\Delta x' = \Delta x/N_x$, $\Delta y' = \Delta y/N_y$ and $\Delta z' = \Delta z/N_z$. The values of N_x, N_y, N_z are equally set as 20 in this study. We count the number of smaller cells inside the solid, denoted as $N^s_{i,j,k}$. Then, the value of solid volume fraction at node (i, j, k) can be determined by $\eta_{i,j,k} = \frac{N^s_{i,j,k}}{N_x N_y N_z}$.

3.3.2. Projection method

We separate the temporal and spatial derivative terms, and discretize the temporal terms in Eq. (71) by using the second-order Adams-Bashforth scheme. Then, we can obtain the following equation

$$\frac{\mathbf{u}^{n+1} - \mathbf{u}^n}{\Delta t} + \left(\frac{3}{2}\mathbf{A}^n - \frac{1}{2}\mathbf{A}^{n-1}\right) + \frac{1}{\rho(C)}\nabla p^{n+1} = \eta\mathbf{f}^{n+1}, \tag{73}$$

where

$$\mathbf{A} = (\mathbf{u}\cdot\nabla)\mathbf{u} - \frac{1}{Re}\frac{\nabla\cdot(2\mu(C)\mathbf{D})}{\rho(C)} - \frac{1}{Fr^2}\hat{\mathbf{e}}_g. \tag{74}$$

It should be noted that $\eta = 0$ means that the cell is filled with fluid, so $\mathbf{f}^{n+1} = 0$. If the cell contains any solid $\eta \neq 0$, then the virtual force $\mathbf{f}^{n+1}$ should be considered. First, we omit the presence of solid in the calculation, and calculate the intermediate velocity by

$$\frac{\mathbf{u}^* - \mathbf{u}^n}{\Delta t} + \left(\frac{3}{2}\mathbf{A}^n - \frac{1}{2}\mathbf{A}^{n-1}\right) = 0. \tag{75}$$

After that, the velocity at next time step $\mathbf{u}^{n+1}$ can be obtained by the following equation

$$\mathbf{u}^{n+1} = \mathbf{u}^* - \frac{\Delta t}{\rho(C)}\nabla p^{n+1}. \tag{76}$$

The pressure value p at the $(n+1)$ time level is required to compute the right-hand side of Eq. (76). We take the divergence on both sides of the equation and require that $\nabla\cdot\mathbf{u}^{n+1} = 0$. By this, the following Poisson equation for p^{n+1} is derived:

$$\nabla\cdot\left(\frac{1}{\rho(C)}\nabla p^{n+1}\right) = \frac{\nabla\cdot\mathbf{u}^*}{\Delta t}. \tag{77}$$

Note that Eq. (77) is applied in both water and gas phases. Therefore, no additional treatment on the pressure boundary condition is needed. The Navier-Stokes equations involving only one-phase fluid can be simulated efficiently by a homotopy-wavelet approach [66] or by a cell-elimination method [67].

Expand Eq. (77) into the following difference equation:

$$\underline{\mathbf{a}}p^{n+1}_{i-1,j,k} + \underline{\mathbf{b}}p^{n+1}_{i+1,j,k} + \underline{\mathbf{c}}p^{n+1}_{i,j,k} + \underline{\mathbf{d}}p^{n+1}_{i,j-1,k} + \underline{\mathbf{e}}p^{n+1}_{i,j+1,k} + \underline{\mathbf{f}}p^{n+1}_{i,j,k-1} + \underline{\mathbf{g}}p^{n+1}_{i,j,k+1} = \left(\frac{\nabla\cdot\mathbf{u}^*}{\Delta t}\right)_{i,j,k}, \tag{78}$$

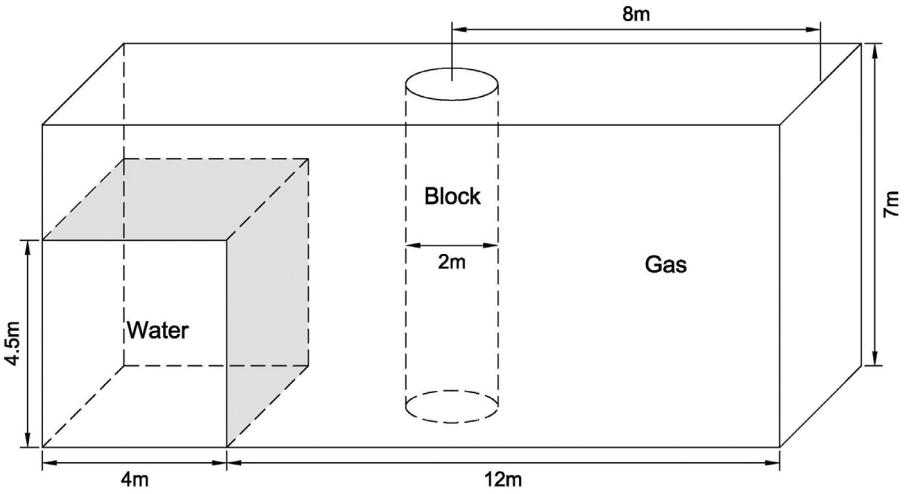

Fig. 26. Sketch of the initial setup for dam-break flow with a circular cylinder obstacle.

where $\underline{\mathbf{a}} = \frac{1}{\rho_{i-1/2,j,k}\Delta x^2}$, $\underline{\mathbf{b}} = \frac{1}{\rho_{i+1/2,j,k}\Delta x^2}$, $\underline{\mathbf{d}} = \frac{1}{\rho_{i,j-1/2,k}\Delta y^2}$, $\underline{\mathbf{e}} = \frac{1}{\rho_{i,j+1/2,k}\Delta y^2}$, $\underline{\mathbf{f}} = \frac{1}{\rho_{i,j,k-1/2}\Delta z^2}$, $\underline{\mathbf{g}} = \frac{1}{\rho_{i,j,k+1/2}\Delta z^2}$, and $\underline{\mathbf{c}} = -(\underline{\mathbf{a}} + \underline{\mathbf{b}} + \underline{\mathbf{d}} + \underline{\mathbf{e}} + \underline{\mathbf{f}} + \underline{\mathbf{g}})$. Use the point-successive over-relaxation method to iterate Eq. (78):

$$P_{i,j,k}^{m+1} = \omega P_{i,j,k}^{m+1} + (1-\omega)P_{i,j,k}^{m}, \tag{79}$$

where the relaxation factor ω is set as 1.5 in this paper. In Eq. (79), m is the number of iterations. Point-wise absolute convergence tolerance is chosen as:

$$|P_{i,j,k}^{m+1} - P_{i,j,k}^{m}| \le 1 \times 10^{-5}. \tag{80}$$

Take the computed pressure value into Eq. (76) and the velocity field $\mathbf{u}^{n+1}$ can then be obtained.

When there is any solid object in the field, the force $\mathbf{f}^{n+1}$ in Eq. (73), which is also called virtual force, must be considered. If the solid is present in a computational cell at node (i, j, k), or, $\eta_{i,j,k} \neq 0$, the velocity field $\mathbf{u}^{n+1}$ should satisfy the no-slip condition on the solid surface $\delta\Omega_s$, that is

$$\mathbf{u}^{n+1} = \mathbf{V}_{\Omega_s}, \text{ on } \delta\Omega_s. \tag{81}$$

In this study, we interpolate the velocity $\mathbf{V}_{\Omega_s}$ on the immersed boundary $\delta\Omega_s$ by using the following equation

$$\mathbf{V}_{\Omega_s} = (1-\eta)\left(\mathbf{u}^* - \frac{\nabla p^{n+1}}{\rho(C)}\Delta t\right) + \eta \mathbf{u}_s, \tag{82}$$

where $\mathbf{u}_s$ is the moving velocity of the solid object. For cases where the solid object is in free-body motion, the virtual force $\mathbf{f}^{n+1}$ can be calculated from Eq. (73). By substituting $\mathbf{V}_{\Omega_s}$ obtained from Eq. (82) into Eq. (73), we can then obtain

$$\mathbf{f}^{n+1} = \frac{\mathbf{u}_s - \mathbf{u}^*}{\Delta t} + \frac{\nabla p^{n+1}}{\rho(C)}. \tag{83}$$

In our study, all the solid objects are set as static, that is, $\mathbf{u}_s = 0$.

3.3.3. Momentum solver and CLSVOF/IB solution procedure

To accurately predict the flow's unidirectional propagation, the second-order upwind scheme is used for calculation of the advection term. Take the term $v\frac{\partial u}{\partial x}$ for example:

$$v\frac{\partial u}{\partial x} = \frac{1}{2\Delta x}(v^+(3u_{i,j,k} - 4u_{i-1,j,k} + u_{i-2,j,k}) + v^-(-u_{i+2,j,k} + 4u_{i+1,j,k} - 3u_{i,j,k})) \tag{84}$$

where $v^+ = \frac{1}{2}(v_{i,j,k} + |v_{i,j,k}|)$ and $v^- = \frac{1}{2}(v_{i,j,k} - |v_{i,j,k}|)$. Other advection terms can be treated in the same way. The second-order center difference scheme is used for the approximation of diffusion terms.

4. Validation studies

To quantify the ability of mass conservation and fluid-fluid interface involving large interface distortions for dam-break problems, the present CLSVOF method is compared with the LS method [19]. The mass error is defined as

$$\mathbf{M}_{error} = \frac{\int C(t)\ d\Omega - \int C(t=0)\ d\Omega}{\int C(t=0)\ d\Omega}. \tag{85}$$

Table 1 lists the grid and time-step sizes used in all the dam-break flow problems. Unit grid ($\equiv \frac{1}{h}$) is defined as the number of cells per unit length, and $h = \Delta x = \Delta y = \Delta z$ is the spacing between grid points.

4.1. 2D Dam-break flow

To understand the influence of the choice of η introduced in Eq. (24) on the resulting position of the interface, and on the matching with the LS interface following Eq. (26), 2D dam-break flow is simulated. The fluid properties are considered to be the same as those given in Ref. [68]. The results for this case are predicted at $Re = 42792$ in a computational domain of 5.0×2.5. No-slip boundary condition is imposed on all walls.

The red solid line and black dashed line in Fig. 2(a) indicate the LS and VOF interfaces solved by LS and VOF methods without considering η. We could tell that the two interfaces are quite different. Fig. 2(b) shows the LS and VOF interfaces with η considered, and the two interfaces agree well with each other. η is considered in the reconstruction procedure for the following reasons. Normal vectors are needed in the WLIC method, which are calculated using the level set function (see Eq. (55)). If η was not considered, the level set interface would not have coincided with the VOF interface (Fig. 2(a)), which means that the normal vectors of the VOF interface are not calculated using the "correct" level set function. If η is considered, however, we would be able to use the "correct" level set function to calculate the normal vectors.

In the CLSVOF algorithm (see Section 2.3), computational cost increases if the reconstruction procedure between ϕ and C is adopted. If reconstruction was adopted in each time step in the present algorithm, there could be extremely high computational cost although it ensures accurate interface capturing. We compared the mass conservation performance and Central Processing Unit (CPU) time cost of four strategies: reconstruction in each 5, 10, 15, and 20 time steps. Results in Fig. 3 and Table 2 show that the computation time is reduced and mass loss results remain almost the same as reconstruction is implemented at greater time intervals. However, convergence is not reached. As this manuscript already takes up much space, we will spare more validation studies in future researches and will propose a convergence principle. In this study, the mass results reconstructed every 10 time steps and every 5 time steps are the best. Computation every 10 time steps takes less time, so this one is adopted.

4.2. 3D Dam-break flow

Dam-break problems have been intensively investigated and its variations are analyzed in Refs. [69–71]. Martin and Moyce (1952) provided an experimental basis for comparison [71]. Their experiment setup is a water column with height $1.25a$ and width a, which is specified in a rectangular $5a \times a \times 1.25a$ domain. This water column suddenly collapses over a horizontal surface due to gravity. We simulate this **case A** for $a = 0.0571$m and **case B** for $a = 0.1143$m, respectively.

The influence of grid size on simulation results is tested by using $h = \frac{1}{20}$, $\frac{1}{30}$ and $\frac{1}{40}$. Instantaneous snapshots of the interface for **case A** and **case B** at different instants are presented in Fig. 4(a)-(f) and Fig. 5(a)-(f), respectively. It can be seen that the dam-break flow hits against the vertical right side wall and then starts rising upwards along the right side wall at $t = 3.75$ for both cases. Comparison between experimental results and the present numerical results of non-dimensional surge front location and the water column height for **case A** are plotted in Fig. 6(a) and (b), respectively. For **case B**, the surge front location is plotted versus time in Fig. 7. The last three points remain still in Figs. 6(a) and 7. This is because the surge front reaches the end of the flume (with a dimensionless length of 5) at around $t = 2.6$ and does not move any forward. The mass loss results using the present CLSVOF and LS methods are shown in Fig. 8. As is shown in Fig. 8, we observe serious mass loss in the LS method.

4.3. Dam-break flow over a wet bed

The initial stage of dam-break flow over a wet bed which has important applications in water resources and hydropower engineering is simulated by the proposed numerical model. This dam-break flow experiment was conducted by Jánosi et al. [72] in a 10.33m long, 0.15m high flume with a flat bed. A water body with depth of 0.15m was kept using a vertical baffle plate located 0.38m downstream of the upper end. Note that the initial water depth in the reservoir was 0.018m. The initial condition for the velocity components are set to zero everywhere, and the pressure distribution is defined to be hydrostatic pressure relative to the top surface of the computational domain. Boundary conditions for all the six edges are set as free slip walls. The present numerical results are shown in Fig. 9 for interface evolution at different instants. As shown in Fig. 9 (e), the dam-break flow over the wet bed is rolling and mixing with the water in the downstream and entraining air bubbles, respectively. Comparison with the experiments of Jánosi et al. [72] is provided in Fig. 10. One can observe that the interface predicted using the proposed CLSVOF method is not satisfactory enough. According to the literature [73], the differences between experiments and simulations could be attributed to the fact that the movement of gate is considered in experiments but is neglected in simulation. We will take the size and movement of gate into consideration in future studies to improve the present method. Fig. 11 shows that mass is better preserved compared with LS method.

5. Numerical results

Dam-break flows impacting various stationary obstacles is investigated by tracking the moving interface between the two immiscible gas-liquid fluids and treating gas-fluid-solid problems using the proposed CLSVOF/IB method. The computational

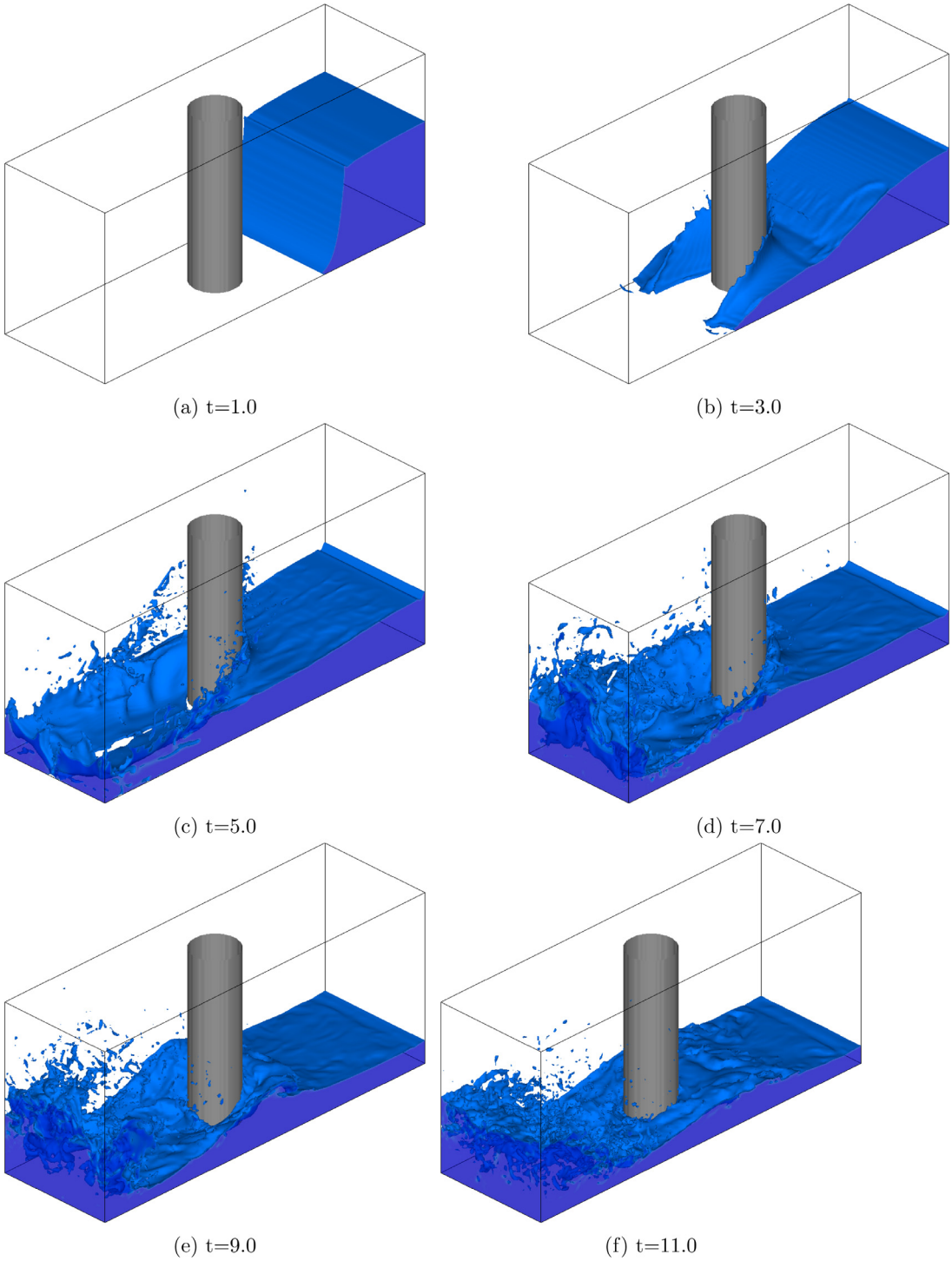

Fig. 27. Numerical results of dam-break flow over an cylinder obstacle solved by present method with mesh size $h = \frac{1}{15}$ and time step $\Delta t = 0.01h$.

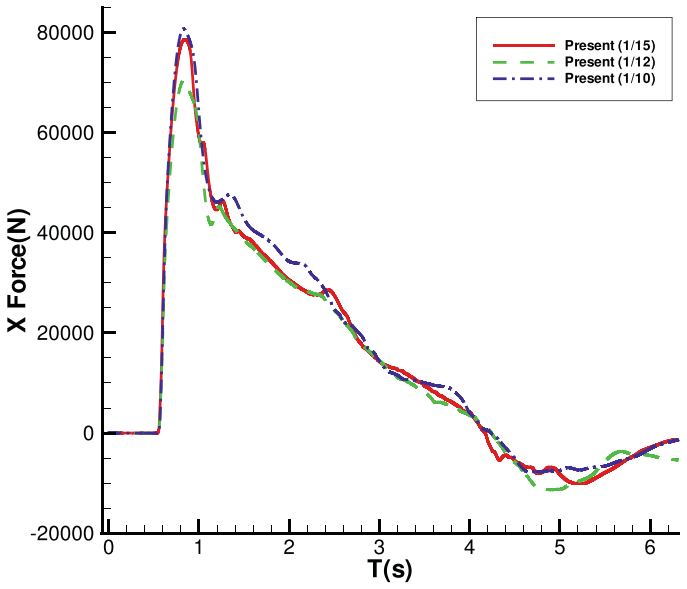

(a)

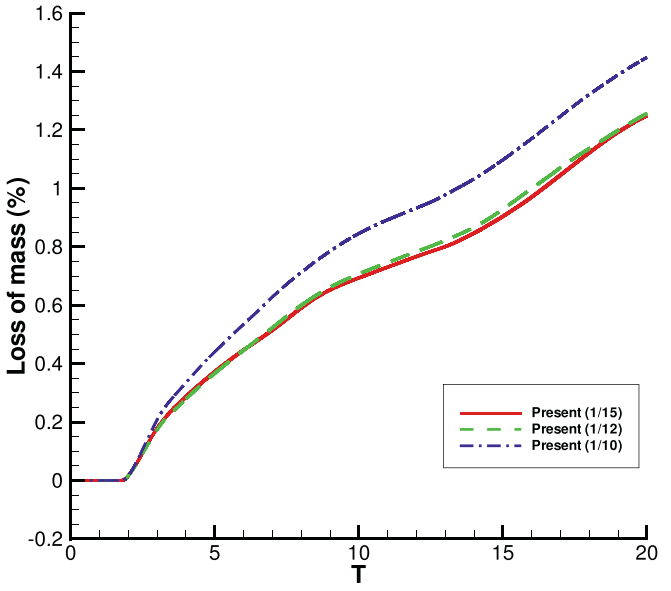

(b)

Fig. 28. (a)Evolution of x force acting on the cylinder using present method with different mesh size. (b) Mass loss evolution using present method with different mesh size.

efficiency of the following four dam-break problems is tested using an INTEL Core(TM) i7-4930K, 3.40 GHz computer. The computational time for different mesh sizes is evaluated in Table 3.

5.1. Dam-break flow with a short obstacle

In Ref. [31], a 0.55m high water column initially at rest suddenly collapses due to gravity to form a dam-break flow and interacts with a rectangular obstacle placed downstream of the flow in a tank. The computational domain is a 3.22m long, 1.0m wide and 1.0m high water tank. At the back end of the tank is the 0.4m long, 0.2m wide and 0.2m high obstacle. The geometry of the tank together with placement of the obstacle is shown in Fig. 12. Four vertical height probes $H_1 \sim H_4$ are used, with one in the reservoir and the other three in the tank, as can be seen in Ref. [31]. $\frac{1}{20}$, $\frac{1}{30}$ and $\frac{1}{40}$ mesh sizes are

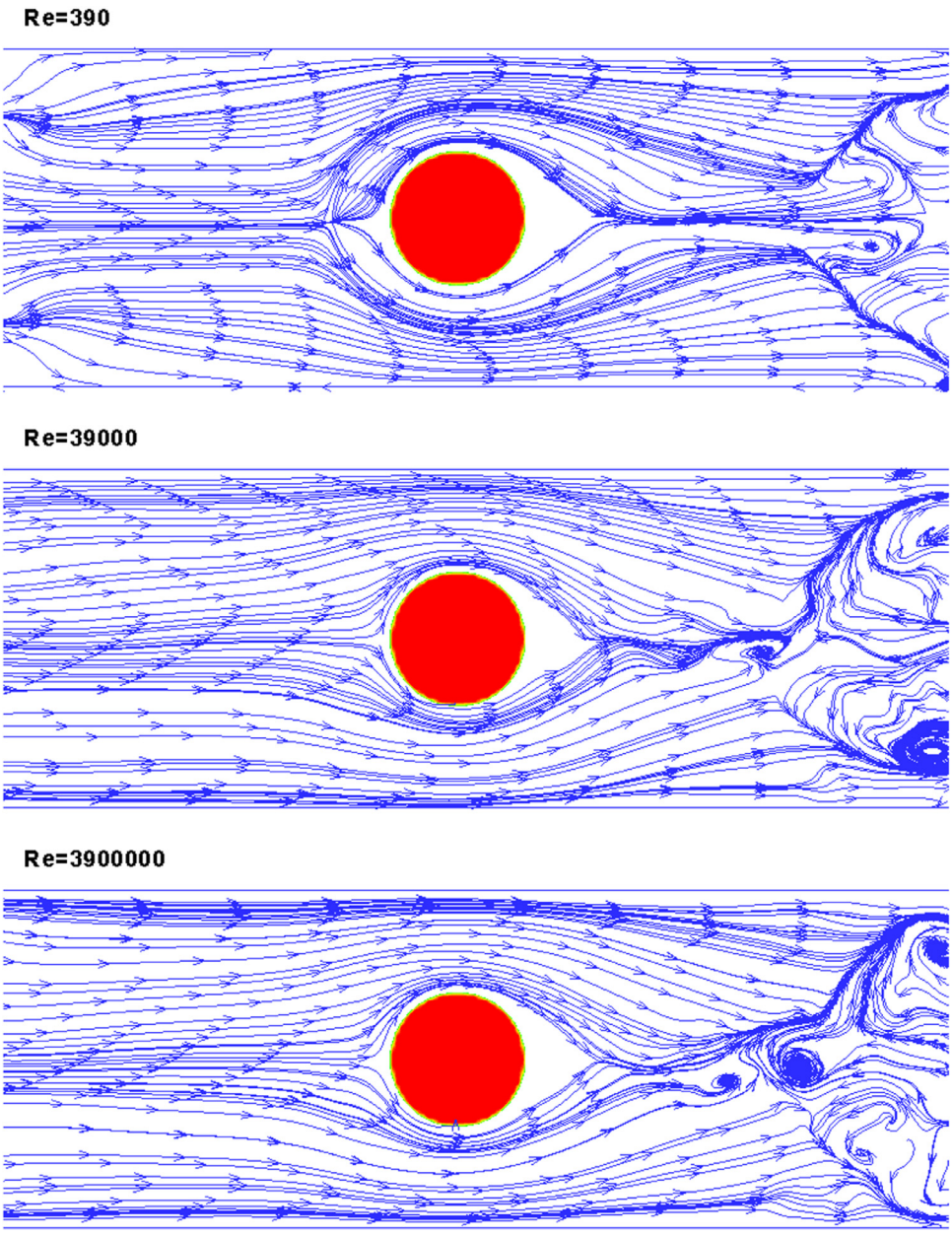

Fig. 29. Predicted streamlines at $t = 10$ on the slice of $z = 0.2$ of the problem of dam-break flow over an cylinder obstacle of different Reynolds number.

adopted for simulation. Free-slip conditions are applied on all walls in the simulation, including the one on the top of the tank.

Figs. 13 –15 present the time evolution of the free surface at several instants where coarse and fine mesh results are shown together for comparison. As can be seen, hardly any difference can be found in the coarse and fine mesh computation results when the dam-break flow first impacts the object. After the impact at $t = 2.60$, however, the run-up is significantly higher for the finest mesh case when the water runs up the back wall of the computational domain. While the three meshes provide very similar flow features in general, the fine mesh allows for better resolution of the free-surface fine-scale features including wave breaking. Good agreement at locations $H_1 \sim H_4$ can be identified from the numerical results [31] in Fig. 16. We find that the mass is well conserved in $\frac{1}{20}$, $\frac{1}{30}$ and $\frac{1}{40}$ mesh sizes, so in fact the results are almost the same (Fig. 16). The results computed with the finest mesh size $\frac{1}{40}$ appear better because it presents details in finer mesh. Fig. 17 shows that the mass is better preserved compared with the LS method. Although the LS method can handle flow processes with complex topological changes including breakup and coalescence of the dam-break flow, it suffers severe numerical dissipation because of the hyperbolic properties of the level set equation, which usually leads to mass loss.

5.2. Dam-break flow with a tall obstacle

The problem under investigation is of a dam-break flow impacting a tall vertical square obstacle. The computational domain is a 1.6m long, 0.61m wide and 0.3m tall water tank. A 0.4m wide, 0.3m tall water column placed at the front end of the tank collapses under the action of gravity, and then impacts a tall obstacle in the middle of the tank. Besides, a layer of water approximately 1cm deep is initially present on the bottom of the tank. The detailed placement of this problem is described in Fig. 18. The free-surface snapshots at $t = 2, 4, 6, 8, 10$ and $t = 12$ are shown in Fig. 19. In this figure, before impacting the downstream structure, the front of the downstream wave already displays slight instabilities; after impacting, significant instabilities are observed. The spatial asymmetry in the flow field is present due to both the truncation errors induced from difference of the Navier-Stokes equations, and errors from the SOR method used when solving the pressure Poisson equation. Because of these errors, the velocity field obtained is asymmetric. Advection of the free surface equation using the asymmetric velocity field produces asymmetry in the free surface.

The predicted numerical results of x-force are compared with the numerical results by Marrone et al. [74] in Fig. 20 and good agreement can be seen between the simulation and experiment. The mass error is calculated by the present CLSVOF method on different grids, as shown in Fig. 21. Although the proposed CLSVOF method has its major advantages of rigorous mass conservation and conservative discretization, CLSVOF methods suffer from the occurrence of “flotsam” and “jetsam”, which are small remnants of mixed-fluid zones and may lead to mass loss.

5.3. Dam-break flow with an oblique obstacle

The proposed CLSVOF method is further validated using an experiment carried out by Soares-Frazão and Zech [3]. In their experiment, a dam-break flow impacting a rectangular obstacle was investigated employing several different measurements including the water level evolution measured by water level gauges and the velocity measured by an acoustic Doppler velocimeter. The channel under investigation is about 36m long, 3.6m wide with a rectangular cross section except near the bed, where this section is cut to form a trapezoidal shape. The reservoir is about 6.9m long. The obstacle is 0.80m long and 0.40m wide, and is obliquely placed in the channel. A gate separates the upstream part of the channel, representing the reservoir, from the downstream part, representing the valley. The gate is located between two impermeable fixed blocks and the cross section between those abutments is rectangular and narrower than the channel cross-section. The dimensions of the channel and obstacle and the detailed placement are shown in Fig. 22.

The exact coordinates of the four corners of the oblique obstacle according to the origin of the axes are indicated in Table 4. The origin of the axes is taken at the center of the gate, with positive x-direction towards the downstream end of the channel. The initial water depth in the upstream reservoir is $h_0 = 0.40$m and there was initially a thin layer of 0.02m water in the channel. The water level is measured by four water-level gauges located in the channel as indicated in Fig. 23: one gauge in the reservoir to monitor its emptying and thus the inflow discharge, and the others around the oblique obstacle. Their exact position is given in Table 5. Snapshots of the gas/liquid phases' time evolution are shown in Fig. 24. The water height compared with experiment data at gates $G1$, $G2$, $G4$, $G6$ are plotted in Fig. 25. The different behaviors make sense since the gauges are located asymmetrically, as is also present in Ref. [3]. The hydraulic jump produced by reflection against the oblique obstacle does not reach the gauges simultaneously.

5.4. Dam-break flow with a cylinder obstacle

A three-dimensional dam-break wave interacting with a circular cylinder obstacle is considered in this section. The 16m long, 5m wide and 7m high water tank is taken as the computational domain, where a water column of $4\text{m} \times 5\text{m} \times 4.5\text{m}$ is initially placed behind a vertical plate. In the middle of the tank there is a circular cylinder of radius $r = 1$m and height $h =$ 7m. Fig. 26 presents a sketch of the initial setup. Fig. 27 shows a sequence of snapshots of the free surface wave evolution. An horseshoe pattern at $t = 3$ can be seen in front of the vertical cylinder obstacle. The evolution downstream of the obstacle at $t = 7.0$ is complex and disordered. The disordered evolution is because of the interaction between the upstream flow diverting at the cylinder obstacle and the downstream flow reflected after hitting the left wall. Fig. 28(a) the time history of the horizontal force acting on the cylinder and a mass conservation test has also been performed for this case in Fig. 28(b). As can be seen in Fig. 28(b), mass is not well conserved after $t = 2$. This is because the flow hit the cylinder obstacle tempestuously which produces the “flotsam” and “jetsam”.

The streamline in the case with a cylinder obstacle presented in Fig. 29 with Reynolds numbers 390, 39000 and 3900000. In $Re = 390$, a symmetric and steady wake is predicted behind the cylinder. The cylinder wake instabilities can be observed at $Re > 390$. As fluid flows over solid under low Reynolds numbers, the flow is viscous force-dominated and tends to form a steady state, where symmetry is present. The separation of boundary layer is absent as well and therefore no vortex is formed, or only a pair of trailing vortex is present. As Reynolds number increases, the flow tends to be inertial force-dominated and becomes unstable. Turbulence occurs and the flow field becomes asymmetrical. Besides, we consider the numerical method as another reason for asymmetry under high Reynolds numbers, but not the main one. Under high Reynolds numbers, discretization errors derive mainly from the advection terms in Navier-Stokes equations. The second-order upwind scheme is used for calculation of the advection term in this study. Discretization schemes with lower order accuracy derives larger truncation errors and presents asymmetrical flow fields.

6. Concluding remarks

In this study, a CLSVOF/IB method is developed to simulate dam-break flow impacting downstream obstacles. A variety of dam-break flows have been numerically investigated with specific interests on local loads on structures impacted by the flow, measurement of the water level, and prediction of mass loss. In the proposed CLSVOF method, VOF function is solved under the framework of THINC/WLIC, and LS function is solved directly from its advection equation. Numerical errors introduced in the computation of advection equation may result from LS and VOF having two different geometries. Because of this, the solution may diverge and become unstable. To make sure the LS function is correctly connected to the identical geometry described by the VOF function, we adopted a relatively simple algorithm, where the reinitialization procedure of LS from the reconstruction of VOF is not required. In the present IB method, momentum forcing terms are calculated using the volume fraction of solid on the body surface, which is easy for extension to three-dimensional cases.

The proposed CLSVOF/IB method yields accurate solutions such as water level and horizontal force acting on the structure in comparison with experimental or numerical results available in the literature. In addition, this coupled method improves the mass conservation performance compared to LS methods. We have noticed a non-monotone behaviour of the mass loss with grid spacing h, which indicates that mass convergence is not yet achieved, and that a grid sensitivity analysis is needed. As the computed water level results agree well with experimental measurements in Section 5.1 and consequently so does the force in the x-direction in Section 5.2, we did not conduct any further analysis. We also find that in non-submerged cases, the dam-break flow hits the obstacles and becomes much more transient than in submerged cases, because increased nonlinearity that follows increases mass loss in computation. The weaknesses of this method is that CLSVOF is computationally costlier than LS. This is because in LS methods, only the LS advection equation is solved, while in CLSVOF methods, both VOF and LS advection equations are solved. In future studies, high performance parallel computing may be introduced to improve the efficiency. Sediment transport can also be considered to discuss the influence of dam-break flow and sediment release on downstream ecology.

Acknowledgements

This study is financially supported by National Natural Science Foundation of China (No. 91547211), National Natural Science Foundation of China (No. 51579164), Fundamental Research Funds for the Central Universities (No. YJ201837), Department of Science and Technology of Sichuan Province (No. 2019YJ0118), and Innovation spark project (No. SCUH0049).

Appendix

Discret integration function for two and three dimensional cases

In 2D case, the integration area Ω_{ij} in Fig. 30(a) is indicated in blue

$$\Omega_{ij} = \left((x,y)|x_{i-1/2} < x < x_{i+1/2} \quad \text{and} \quad y_{j-1/2} < y < y_{j+1/2}\right). \tag{86}$$

Function values at the centre O and the eight adjacent points are also indicated in Fig. 30(a). The integration over Ω_{ij} can be expressed as the sum of the eight sub areas:

$$\begin{aligned}\int_{\Omega_{ij}} g d\Omega \quad &= g_{OAB}S_{\Delta OAB} + g_{OBC}S_{\Delta OBC} + g_{OCD}S_{\Delta OCD} + g_{ODE}S_{\Delta ODE} + \\ &g_{OEF}S_{\Delta OEF} + g_{OFG}S_{\Delta OFG} + g_{OGH}S_{\Delta OGH} + g_{OHA}S_{\Delta OHA}.\end{aligned} \tag{87}$$

Approximation to $g_{OAB}S_{\Delta OAB}$ is

$$g_{OAB}S_{\Delta OAB} \approx \frac{1}{3}(g_O + g_A + g_B)\cdot\frac{1}{2}\cdot\frac{1}{2}h\cdot\frac{1}{2}h, \tag{88}$$

where h is grid spacing and

$$g_O = g(i,j), \tag{89}$$

$$g_A \approx \frac{g(i,j) + g(i-1,j+1)}{2}, \tag{90}$$

$$g_B \approx \frac{g(i,j) + g(i,j+1)}{2}. \tag{91}$$

Integration over the other seven areas can be derived similarly. Then, Eq. (87) can be expressed as

$$\int_{\Omega_{ij}} g d\Omega = \frac{1}{24}h^2\left(16g(i,j) + \sum_{m,n=-1;(m,n)\neq(0,0)}^{1} g_{i+m,j+n}\cdot\right) \tag{92}$$

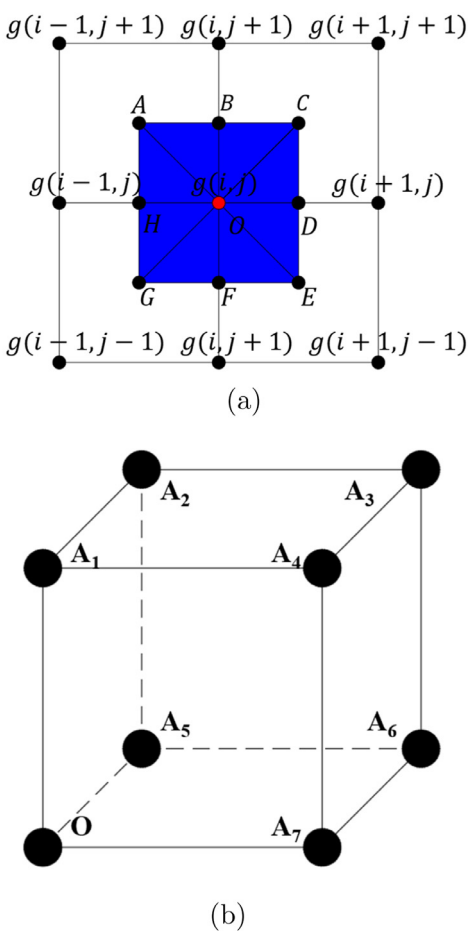

Fig. 30. The diagrammatic sketch of integration area (a) 2D case; (b) 3D case.

In 3D case, the cubic integration area is

$$\Omega_{ijk} = \left((x,y)|x_{i-1/2} < x < x_{i+1/2} \quad \text{and} \quad y_{j-1/2} < y < y_{j+1/2} \quad \text{and} \quad z_{k-1/2} < z < z_{k+1/2}\right). \tag{93}$$

The cubic area can be subdivided into eight equivalent sub-cubic areas. Function value at the cubic centre O is noted as $g(i, j, k)$. Fig. 30(b) shows one of the eight sub-cubic areas. And we have

$$V_{OA_1A_2A_3A_4A_5A_6A_7} = V_{OA_1A_2A_3} + V_{OA_5A_2A_3} + V_{OA_1A_4A_3} + V_{OA_7A_4A_3} + V_{OA_5A_6A_3}, \tag{94}$$

where $V_{OA_1A_2A_3A_4A_5A_6A_7}$ denotes the volume of $OA_1A_2A_3A_4A_5A_6A_7$. We denote the point that is one grid away from O as O_1, the point that is $\sqrt{2}$ grids away from O as O_2, the point that is $\sqrt{3}$ grids away from O as O_3, the point that is $\frac{1}{2}$ grid away from O as $O_{1/2}$, the point that is $\frac{\sqrt{2}}{2}$ grid away from O as $O_{2/2}$, and the point that is $\frac{\sqrt{3}}{2}$ grids away from O as $O_{3/2}$. Function value at O_1 is denoted as g_{O_1}, and other notations are similarly defined.

Due to the symmetry, integration over the entire cubic area is

$$\int_{\Omega_{ijk}} g d\Omega = \frac{1}{8}\cdot\frac{1}{6}\cdot\frac{1}{4}h^3\left(8\cdot 6\cdot g_O + 4\cdot 2\cdot 6 g_{O_{1/2}} + 2\cdot 2\cdot 12 g_{O_{2/2}} + 1\cdot 6\cdot 8 g_{O_{3/2}}\right). \tag{95}$$

Since $O_{1/2}$, $O_{2/2}$, $O_{3/2}$ are the mid points of $\overline{OO_1}$, $\overline{OO_2}$, $\overline{OO_3}$, function values at the three points can be expressed as

$$g_{O_{i/2}} \approx \frac{g_{O_i} + g_O}{2}, \quad \text{for } i = 1, 2, 3. \tag{96}$$

Therefore,

$$\begin{aligned} \int_{\Omega_{ijk}} g d\Omega = \tfrac{1}{8}\cdot\tfrac{1}{6}\cdot\tfrac{1}{4}h^3 \quad & \left(6\cdot 8\cdot g_O + 4\cdot 6\cdot g_O + 2\cdot 12\cdot g_O + 3\cdot 8\cdot g_O \right. \\ & \left. + 4\cdot 6\cdot g_{O_1} + 2\cdot 12\cdot g_{O_2} + 1\cdot 3\cdot 8\cdot g_{O_3}\right). \end{aligned} \tag{97}$$

The sum of weights at the 26 adjacent points is

$$\sum_{m,n,l=-1;(m,n,l)\neq(0,0,0)}^{1} g_{i+m,j+n,k+l} = 6g_{O_1} + 12g_{O_2} + 8g_{O_3}. \tag{98}$$

Then, the integration can be expressed as

$$\int_{\Omega_{ijk}} g d\Omega = \frac{1}{96}h^3\left(60g(i,j,k) + \sum_{m,n,l=-1;(m,n,l)\neq(0,0,0)}^{1} g_{i+m,j+n,k+l} + 6g_{O_1} + 4g_{O_3}\right), \tag{99}$$

or

$$\int_{\Omega_{ijk}} g d\Omega = \frac{1}{64}h^3\left(40g(i,j,k) + \sum_{m,n,l=-1;(m,n,l)\neq(0,0,0)}^{1} g_{i+m,j+n,k+l} + 2g_{O_1} - 4g_{O_2}\right). \tag{100}$$

Considering

$$g(i+1,j,k) + g(i-1,j,k) \approx 2g(i,j,k), \tag{101}$$

Eqs. (99)–(100) can be approximated as

$$\int_{\Omega_{ijk}} g d\Omega = \frac{1}{48}h^3\left(35g(i,j,k) + \sum_{m,n,l=-1;(m,n,l)\neq(0,0,0)}^{1} g_{i+m,j+n,k+l}\right), \tag{102}$$

and

$$\int_{\Omega_{ijk}} g d\Omega = \frac{1}{32}h^3\left(19g(i,j,k) + \sum_{m,n,l=-1;(m,n,l)\neq(0,0,0)}^{1} g_{i+m,j+n,k+l}\right). \tag{103}$$

Define

$$\int_{\Omega_{ijk}} g d\Omega \approx \frac{1}{\mathbf{n}+26}h^3\left(\mathbf{n}\ g(i,j,k) + \sum_{m,n,l=-1;(m,n,l)\neq(0,0,0)}^{1} g_{i+m,j+n,k+l},\right), \tag{104}$$

where $\mathbf{n}$ is unknown value. Compare Eq. (104) with the weighted average of Eqs. (102) and (103), we have $\mathbf{n} = 51$. Substitute $\mathbf{n} = 51$ into Eq. (104), the Eq. (11) is therefore obtained

$$\int_{\Omega_{ijk}} g d\Omega \approx \frac{1}{77}h^3\left(51g(i,j,k) + \sum_{m,n,l=-1;(m,n,l)\neq(0,0,0)}^{1} g_{i+m,j+n,k+l}\right) \tag{105}$$

References

[1] Tang HS, Keen TR, Khanbilvardi R. A model-coupling framework for nearshore waves, currents, sediment transport, and seabed morphology. Commun Nonlinear Sci Numer Simulat 2009;14:2935–47.
[2] Wang JY, Tang HS, Fang HW. A fully coupled method for simulation of wave-current-seabed systems. Commun Nonlinear Sci Numer Simulat 2013;18:1694–709.
[3] Soares-Frazão S, Zech Y. Experimental study of dam-break flow against an isolated obstacle. J Hydraul Res 2007;45:27–36.
[4] Marsooli R, Wu W. 3-D finite-volume model of dam-break flow over uneven beds based on VOF method. Adv Water Resou 2014;70:104–17.
[5] Ng KC, Hwang YH, Sheu TWH, Yu CH. Moving particle level-set (MPLS) method for incompressible multiphase flow computation. Comput Phys Commun 2015;196:317–34.
[6] Park KM, Yoon HS, Kim MI. CFD-DEM based numerical simulation of liquid-gas-particle mixture flow in dam break. Commun Nonlinear Sci Numer Simulat 2018;59:105–21.
[7] Larocque LA, Imran J, Chaudhr MH. 3D numerical simulation of partial breach dam-break flow using the LES and $k-\epsilon$ turbulence models. J Hydraul Res 2013;51(2):145–57.
[8] Aureli F, Dazzi S, Maranzoni A, Mignosa P, Vacondio R. Experimental and numerical evaluation of the force due to the impact of a dam-break wave on a structure. Adv Water Resou 2015;76:29–42.
[9] Wang Z, Tong AY. A sharp surface tension modeling method for two-phase incompressible interfacial flows. Int J Numer Meth Fluid 2010;64(7):709–32.
[10] Yang J, Stern F. Sharp interface immersed-boundary/level-set method for wave-body interactions. J Comput Phys 2009;228:6590–616.
[11] Wang Z, Yang J, Koo B, Stern F. A coupled level set and volume-of-fluid method for sharp interface simulation of plunging breaking waves. Int J Multiphas Flow 2009;35:227–46.
[12] Rauschenberger P, Criscione A, Eisenschmidt K, Kintea D, Jakirlić S, Tuković Ž, Roisman IV, Weigand B, Tropea C. Comparative assessment of volume-of-fluid and level-set methods by relevance to dendritic ice growth in supercooled water. Comput Fluids 2013;79:44–52.
[13] Hirt CW, Nichols BD. Volume of fluid (VOF) method for the dynamics of free boundaries. J Comput Phys 1981;39:201–25.
[14] Wang Z, Yang J, Stern F. A new volume-of-fluid method with a constructed distance function on general structured grids. J Comput Phys 2012;231:3703–22.
[15] Zeng L, Luo ZL, Chen B, Yang ZF, Li Z, Lin WX, Chen GQ. Numerical analysis of a lock-release oil slick. Commun Nonlinear Sci Numer Simulat 2010;15:2222–30.
[16] Osher S, Sethian JA. Fronts propagating with curvature dependent speed: algorithms based on hamilton-jacobi formulations. J Comput Phys 1988;79:12–49.
[17] Sussman M, Smereka P, Osher S. A level set approach for computing solutions to incompressible two-phase flow. J Comput Phys 1994;114(1):146–59.

[18] Sussman M, Almgren AS, Bell JB, Colella P, Howell LH, Welcome ML. An adaptive level set approach for incompressible two-phase flows. J Comput Phys 1997;148(1):81–124.
[19] Sussman M, Fatemi E. An efficient, interface-preserving level set redistancing algorithm and its application to interfacial incompressible fluid flow. Siam J Sci Comput 1999;20(4):1165–91.
[20] Yokoi K. A variational approach to multi-phase motion of gas, liquid and solid based on the level set method. Comput Phys Commun 2000;180(7):1145–9.
[21] Chung MH. An adaptive cartesian cut-cell/level-set method to simulate incompressible two-phase flows with embedded moving solid boundaries. Comput Fluids 2013;71:469–86.
[22] Katiyar G, Karagadde S, Saha SK, Sharma A. Numerical modelling of bubble growth in microchannel using level set method. Int J Heat Mass Transfer 2016;101:719–32.
[23] Ki H. Level set method for two-phase incompressible flows under magnetic fields. Comput Phys Commun 2010;181(6):999–1007.
[24] Choi M, Son G, Shim W. A level-set method for droplet impact and penetration into a porous medium. Comput Fluids 2017;145:153–66.
[25] Raessi M, Pitsch H. Consistent mass and momentum transport for simulating incompressible interfacial flows with large density ratios using the level set method. Comput Fluids 2012;63:70–81.
[26] Luo K, Shao CX, Yang Y, Fan JR. A mass conserving level set method for detailed numerical simulation of liquid atomization. J Eng Thermophys-Rus 2015;298:495–519.
[27] Moghadam AM, Shafieefar M, Panahi R. Development of a high-order level set method: compact conservative level set (CCLS). Comput Fluids 2016;129:79–90.
[28] Olsson E, Kreiss G. A conservative level set method for two phase flow. J Comput Phys 2005;210(1):225–46.
[29] Shao C, Luo K, Yang J, Chen S, Fan J. Accurate level set method for simulations of liquid atomization. Chinese J Chem Eng 2015;23:597–604.
[30] Chai M, Luo K, Shao C, Chen S, Fan J. DNS analysis of incipient drop impact dynamics using an accurate level set method. Chinese J Chem Eng 2017;25:1–10.
[31] Kees CE, Akkerman I, Farthing MW, Bazilevs Y. A conservative level set method suitable for variable-order approximations and unstructured meshes. J Comput Phys 2011;230(12):4536–58.
[32] Zhao L, Mao J, Bai X, Liu X, Li T, Williams JJR. Finite element implementation of an improved conservative level set method for two phase flow. Comput Fluids 2014;100:138–54.
[33] Enright D, Fedkiw R, Ferziger J, Mitchell I. A hybrid particle level set method for improved interface capturing. J Comput Phys 2002;183(1):83–116.
[34] Wang Z, Yang J, Stern F. An improved particle correction procedure for the particle level set method. J Comput Phys 2009;228:5819–37.
[35] Sun D, Tao W. A coupled volume-of-fluid and level set (VOSET) method for computing incompressible two-phase flows. Int J Heat Mass Tran 2010;53(4):645–55.
[36] Wang T, Li H, Feng Y, Shi D. A coupled volume-of-fluid and level set (VOSET) method on dynamically adaptive quadtree grids. Int J Heat Mass Tran 2013;67(4):70–3.
[37] Ling K, Li Z, Sun D, He Y, Tao W. A three-dimensional volume of fluid & level set (VOSET) method for incompressible two-phase flow. Comput Fluids 2015;118:293–304.
[38] Cao Z, Sun DL, Yu B, Wei J. A coupled volume-of-fluid and level set (VOSET) method based on remapping algorithm for unstructured triangular grids. Int J Heat Mass Tran 2017;111:232–45.
[39] Sussman M, Pucket EG. A coupled level set and volume of fluid method for computing 3d and axisymmetric incompressible two-phase flows. J Comput Phys 2000;162:301–37.
[40] Sussman M. A second order coupled level set and volume-of-fluid method for computing growth and collapse of vapor bubbles. J Comput Phys 2003;187:110–36.
[41] Son G, Hur N. A coupled level-set and volume-of-fluid method for the buoyancy-driven motion of fluid particles. Numer Heat Transfer, Part B:Fundam 2002;42:523–42.
[42] Son G. Efficient implementation of a coupled level-set and volume-of-fluid method for three-dimensional incompressible two-phase flows. Numer Heat Transfer, Part B 2003;43:549–5652.
[43] Li Q, Ouyang J, Yang B, Li X. Numerical simulation of gas-assisted injection molding using CLSVOF method. Appl Math Model 2012;36:2262–74.
[44] Li S, Chen R, Wang H, Liao Q, Zhu X, Wang Z, He X. Numerical investigation of the moving liquid column coalescing with a droplet in triangular microchannels using CLSVOF method. Sci Bull 2015;60:1911.
[45] Chakraborty I, Biswas G, Ghoshdastidar PS. A coupled level-set and volume-of-fluid method for the buoyant rise of gas bubbles in liquids. Int J Heat Mass Transfer 2013;58(1–2):240–59.
[46] Ningegowda BM, Premachandran B. A coupled level set and volume of fluid method with multi-directional advection algorithms for two-phase flows with and without phase change. Int J Heat Mass Transfer 2014;79:532–50.
[47] Yokoi K, Vadillo D, Hinch J, Hutchings I. Numerical studies of the influence of the dynamic contact angle on a droplet impacting on a dry surface. Phys Fluids 2009;21:072102.
[48] Albadawi A, Donoghue DB, Robinson AJ, Murray DB, Delauré YMC. Influence of surface tension implementation in volume of fluid and coupled volume of fluid with level set methods for bubble growth and detachment. Int J Multiphs Flow 2013;53:11–28.
[49] Koo B, Wang Z, Yang J, Stern F. Impulsive plunging wave breaking down stream of a bump in a shallow water flume. part II:numerical simulations. J Fluids Struct 2012;32:121–34.
[50] Mittal R, Iaccarino G. Immersed boundary methods. Annu Rev Fluid Mech 2005;37:239–61.
[51] Peskin CS. Flow patterns around heart valves: a numerical method. J Comput Phys 1972;10:252–71.
[52] Ghias R, Mittal R, Dong H. A sharp interface immersed bondary method for compressible viscous flows. J Comput Phys 2007;225:528–53.
[53] Fadlun EA, Verzicco R, Orlandi P, Mohd-Yusof J. Combined immersed-boundary methods for three dimensional complex flow simulations. J Comput Phys 2000;161:30–60.
[54] Balaras E, Yang J. Nonboundary conforming methods for large-eddy simulations of biological flows. J Fluid Eng 2005;127:851–5.
[55] Yang J, Preidikman S, Balaras E. A strongly coupled, embedded-boundary method for fluid-structure interactions of elastically mounted rigid bodies. J Fluids Struct 2008;24:167–82.
[56] Zhang C, Lin N, Tang Y, Zhao C. A sharp interface immersed boundary/VOF model coupled with wave generating and absorbing options for wave-structure interaction. Comput Fluids 2014;89:214–31.
[57] Zhang Y, Zou Q, Greaves D, Reeve D, Hunt-Raby A, Graham D, James P, Lv X. A level set immersed boundary method for water entry and exit. Commun Comput Phys 2010;8(2):265–88.
[58] Li Q. Numerical simulation of melt filling process in complex mold cavity with insets using IB-CLSVOF method. Comput Fluids 2016;132:94–105.
[59] Yokoi K. Efficient implementation of THINC scheme: a simple and practical smoothed VOF algorithm. J Comput Phys 2007;226(2):1985–2002.
[60] Xiao F, Honma Y, Kono T. A simple algebraic interface capturing scheme using hyperbolic tangent function. Int J Numer Methods Fluids 2005;48(9):1023–40.
[61] Xiao F, Ii S Ii, Chen C. Revisit to the THINC scheme: a simple algebraic VOF algorithm. J Comput Phys 2011;230(19):7086–92.
[62] Ii S Ii, Sugiyama K, Takeuchi S, Takagi S, Matsumoto Y, Xiao F. An interface capturing method with a continuous function: the THINC method with multidimensional reconstruction. J Comput Phys 2012;231(5):2328–58.
[63] Gu ZH, Wen HL, Yu CH, Sheu TWH. Interface-preserving level set method for simulating dam-break flows. J Comput Phys 2018;374:249–80.
[64] Jiang GS, Peng D. Weighted ENO schemes for hamilton-jacobi equations. Siam J Sci Comput 1997;21(6):2126–43.
[65] Shu CW. Total-variation diminishing time discretizations. SIAM J Sci Stat Comput 1988;9(6):1073–984.

[66] Yu Q, Xu H, Liao S, Yang Z. A novel homotopy-wavelet approach for solving stream function-vorticity formulation of navier-stokes equations. Commun Nonlinear Sci Numer Simulat 2019;67:124–51.
[67] Akbarzadeh P, Derazgisoo SM, Lehdarboni AA. A cell-elimination method for solving steady and unsteady navier-stokes equations. Commun Nonlinear Sci Numer Simulat 2019;69:304–19.
[68] Yue W, Lin C-L, Patel VC. Numerical simulation of unsteady multidimensional free surface motions by level set method. Int J Numer Meth Fluids 2003;42:853–84.
[69] Hu C, Sueyoshi M. Numerical simulation and experiment on dam break problem. J Marine Sci Appl 2010;9(2):109–14.
[70] Chiu PH, Lin YT. A conservative phase field method for solving incompressible two-phase flows. J Comput Phys 2011;230(1):185–204.
[71] Martin JC, Moyce WJ. An experimental study of collapse of liquid columns on a rigid horizontal plane. Trans R Soc London Ser-A 1952;244(882):312–24.
[72] Jánosi IM, Jan D, Szabó KG, Tél T. Turbulent drag reduction in dam-break flows. Exp Fluids 2004;37(2):219–29.
[73] Ye Z, Zhao X. Investigation of water-water interface in dam break flow with a wet bed. J Hydrol 2017;548:104–20.
[74] Marrone S, Antuono M, Colagrossi A, Colicchio G, Touzé DL, Graziani G. δ-SPH model for simulating violent impact flows. Comput Method Appl Mech Engrg 2011;200:1526–42.